EUROPEAN ORGANIZATION FOR NUCLEAR RESEARCH (CERN)

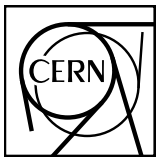

CERN-EP-2020-214
06 November 2020

Measurement of the CKM angle γ and B_s^0-$\overline{B}_s^0$ mixing frequency with $B_s^0 \to D_s^{\mp} h^{\pm}\pi^{\pm}\pi^{\mp}$ decays

LHCb collaboration[†]

Abstract

The CKM angle γ is measured for the first time from mixing-induced *CP* violation between $B_s^0 \to D_s^{\mp} K^{\pm}\pi^{\pm}\pi^{\mp}$ and $\overline{B}_s^0 \to D_s^{\pm} K^{\mp}\pi^{\mp}\pi^{\pm}$ decays reconstructed in proton-proton collision data corresponding to an integrated luminosity of $9\,\text{fb}^{-1}$ recorded with the LHCb detector. A time-dependent amplitude analysis is performed to extract the *CP*-violating weak phase $\gamma - 2\beta_s$ and, subsequently, γ by taking the $B_s^0 - \overline{B}_s^0$ mixing phase β_s as an external input. The measurement yields $\gamma = (44 \pm 12)^\circ$ modulo 180°, where statistical and systematic uncertainties are combined. An alternative model-independent measurement, integrating over the five-dimensional phase space of the decay, yields $\gamma = (44^{+20}_{-13})^\circ$ modulo 180°. Moreover, the $B_s^0 - \overline{B}_s^0$ oscillation frequency is measured from the flavour-specific control channel $B_s^0 \to D_s^- \pi^+\pi^+\pi^-$ to be $\Delta m_s = (17.757 \pm 0.007\,(\text{stat}) \pm 0.008\,(\text{syst}))\,\text{ps}^{-1}$, consistent with and more precise than the current world-average value.

Submitted to JHEP

[†]Authors are listed at the end of this paper.

1 Introduction

Within the Standard Model of particle physics, the charge-parity (CP) symmetry between quarks and antiquarks is broken by a single complex phase in the Cabibbo-Kobayashi-Maskawa (CKM) quark-mixing matrix [1]. The unitarity of this matrix leads to the condition $V_{ud}V_{ub}^* + V_{cd}V_{cb}^* + V_{td}V_{tb}^* = 0$, where V_{ij} are the complex elements of the CKM matrix. This equation can be visualised as a triangle in the complex plane with angles α, β and γ. It is a key test of the Standard Model to verify this unitarity condition by over-constraining the CKM matrix with independent measurements sensitive to various distinct combinations of matrix elements. In particular, measurements of $\gamma \equiv \arg[-(V_{ud}V_{ub}^*)/(V_{cd}V_{cb}^*)]$ in tree-level decays provide an important benchmark of the Standard Model, to be compared with loop-level measurements of γ and other CKM parameters. The world-average value, $\gamma = \left(72.1\,^{+\,4.1}_{-\,4.5}\right)^\circ$ [2,3], is dominated by a combination of LHCb measurements obtained from analyses of beauty meson decays to open-charm final states [4]. Improved direct measurements are needed to set a conclusive comparison to the indirect predictions from global CKM fits, $\gamma = \left(65.7\,^{+\,0.9}_{-\,2.7}\right)^\circ$ [5] or $\gamma = (65.8 \pm 2.2)^\circ$ [6].

This paper presents the first measurement of the CKM angle γ with $B_s^0 \to D_s^\mp K^\pm\pi^\pm\pi^\mp$ decays.[1] The data set is collected with the LHCb experiment in proton-proton (pp) collisions at centre-of-mass energies[2] of 7, 8 and 13 TeV, corresponding to an integrated luminosity of $9\,\text{fb}^{-1}$. In these decays, the interference between $b \to c$ and $b \to u$ quark-level transitions achieved through $B_s^0 - \overline{B}_s^0$ mixing provides sensitivity to the CP-violating weak phase $\gamma - 2\beta_s$ [7,8]. The mixing phase, β_s, is well constrained from $B_s^0 \to J/\psi K^+K^-$ [9,10] and related decays [11–14] and is taken as an external input. The leading-order Feynman diagrams for $B_s^0 \to D_s^- K^+\pi^+\pi^-$ and $\overline{B}_s^0 \to D_s^- K^+\pi^+\pi^-$ decays are shown in Fig. 1. The amplitudes for both processes are of the same order in the Wolfenstein parameter λ [15], $\mathcal{O}(\lambda^3)$, so that interference effects are expected to be large. To account for the strong-phase variation across the phase space of the decay, a time-dependent amplitude analysis is performed. An alternative, model-independent approach analyses the phase-space integrated decay-time spectrum and is pursued as well; this method is conceptually similar to the analysis of $B_s^0 \to D_s^\mp K^\pm$ decays [16,17]. However, a coherence factor needs to be introduced as an additional hadronic parameter, which dilutes the observable CP asymmetry since constructive and destructive interference effects cancel when integrated over the entire phase space. The topologically similar and flavour-specific decay $B_s^0 \to D_s^-\pi^+\pi^+\pi^-$ is used to calibrate detector-induced effects. This mode is also employed to make a precise measurement of the $B_s^0 - \overline{B}_s^0$ mixing frequency, which can be related to one side of the unitarity triangle. The relative branching fraction of these decay modes was measured by LHCb to be $\mathcal{B}(B_s^0 \to D_s^\mp K^\pm\pi^\pm\pi^\mp)/\mathcal{B}(B_s^0 \to D_s^-\pi^+\pi^+\pi^-) = (5.2 \pm 0.5(\text{stat}) \pm 0.3(\text{syst}))\,\%$ [18].

The paper is structured as follows. After introducing the amplitude analysis formalism and the differential decay rates in Sec. 2, the LHCb detector, the event reconstruction and candidate selection are described in Sec. 3. Section 4 presents the measurement of the B_s^0 mixing frequency, followed by the analysis of the $B_s^0 \to D_s^\mp K^\pm\pi^\pm\pi^\mp$ signal channel in Sec. 5. Experimental and model-dependent systematic uncertainties are evaluated in Sec. 6, the results are discussed in Sec. 7, and our conclusions are given in Sec. 8.

[1] Inclusion of charge-conjugate modes is implied throughout except where explicitly stated.
[2] Natural units with $\hbar = c = 1$ are used throughout the paper.

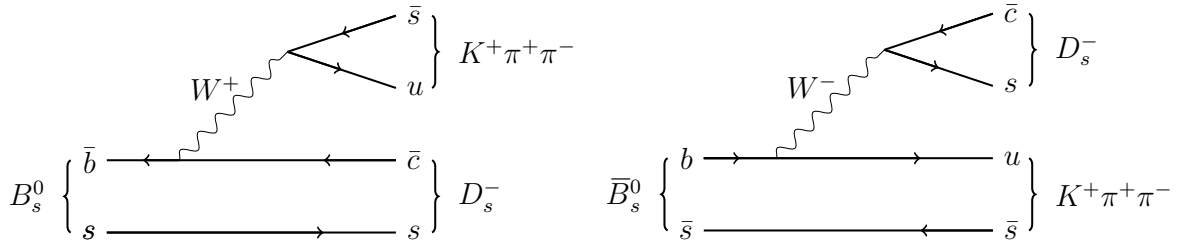

Figure 1: Leading-order Feynman diagrams for (left) B_s^0 and (right) $\overline{B}_s^0$ decays to the $D_s^- K^+\pi^+\pi^-$ final state, where the $\pi^+\pi^-$ subsystem is generically drawn in conjunction with the kaon.

2 Phenomenology of the decay

Assuming tree-level processes are dominant, transitions from B_s^0 and $\overline{B}_s^0$ flavour eigenstates to the final state $f = D_s^- K^+\pi^+\pi^-$ are described by static decay amplitudes

$$\langle f|B_s^0\rangle \equiv A^c(\mathbf{x}), \qquad \langle f|\overline{B}_s^0\rangle \equiv r\, e^{i(\delta-\gamma)}\, A^u(\mathbf{x}), \tag{1}$$

with a relative magnitude r and (constant) strong- and weak-phase differences δ and γ, respectively. A set of five independent kinematic observables (*e.g.* invariant-mass combinations of the final state particles or helicity angles) fully describes the phase space $\mathbf{x}$ of the decay. The hadronic amplitudes $A^c(\mathbf{x})$ and $A^u(\mathbf{x})$, where the superscript c (u) refers to a $b \to c$ ($b \to u$) quark-level transition, contain the strong-interaction dynamics and are given by a coherent sum over intermediate-state amplitudes, $A_i(\mathbf{x})$:

$$A^c(\mathbf{x}) = \sum_i a_i^c\, A_i(\mathbf{x}), \qquad A^u(\mathbf{x}) = \sum_i a_i^u\, A_i(\mathbf{x}). \tag{2}$$

The complex amplitude coefficients a_i^c and a_i^u need to be determined from data. Since the hadronisation process is different for $B_s^0 \to f$ and $\overline{B}_s^0 \to f$ decays, their respective amplitude coefficients are distinct ($a_i^c \neq a_i^u$). To ensure that the parameters r and δ do not depend on the convention employed for the amplitude coefficients, the magnitude squared of the hadronic amplitudes is normalised to unity when integrated over the phase space (with four-body phase-space element $\mathrm{d}\Phi_4$) and the overall strong-phase difference between $A^c(\mathbf{x})$ and $A^u(\mathbf{x})$ is set to zero, *i.e.* $\int |A^c(\mathbf{x})|^2\, \mathrm{d}\Phi_4(\mathbf{x}) = \int |A^u(\mathbf{x})|^2\, \mathrm{d}\Phi_4(\mathbf{x}) = 1$ and $\arg\left(\int A^c(\mathbf{x})^*\, A^u(\mathbf{x})\, \mathrm{d}\Phi_4(\mathbf{x})\right) = 0$. Within this convention, the decay fractions and interference fractions for $b \to c$ ($b \to u$) transitions are defined as

$$F_i^{c(u)} \equiv \int \left| a_i^{c(u)}\, A_i(\mathbf{x}) \right|^2 \mathrm{d}\Phi_4, \qquad I_{ij}^{c(u)} \equiv \int 2\,\mathrm{Re}[a_i^{c(u)}\, a_j^{c(u)*}\, A_i(\mathbf{x}) A_j^*(\mathbf{x})]\, \mathrm{d}\Phi_4. \tag{3}$$

2.1 Amplitude formalism

The isobar model is used to construct the intermediate-state amplitudes $A_i(\mathbf{x})$ [19–21]. Within this model, the four-body decay $B_s^0 \to h_1\, h_2\, h_3\, h_4$ proceeds via two isobar states R_1 and R_2 (typically associated to intermediate resonances), which gives rise to two distinct decay topologies; quasi-two-body decays $B_s^0 \to (R_1 \to h_1\, h_2)\, (R_2 \to h_3\, h_4)$ or cascade

decays $B_s^0 \to h_1\,[R_1 \to h_2\,(R_2 \to h_3\,h_4)]$. The intermediate-state amplitude for a given decay channel i can be parameterised as

$$A_i(\mathbf{x}) = B_{L_{B_s^0}}(\mathbf{x})\,[B_{L_{R_1}}(\mathbf{x})\,T_{R_1}(\mathbf{x})]\,[B_{L_{R_2}}(\mathbf{x})\,T_{R_2}(\mathbf{x})]\,S_i(\mathbf{x})\,, \tag{4}$$

where the form factors B_L account for deviations from point-like interactions and the propagator T_R describes the lineshape of resonance R. The angular correlation of the final state particles subject to total angular momentum conservation is encoded in the spin factor S. The Blatt–Weisskopf penetration factors [22, 23] are used as form factors. They depend on the effective interaction radius $r_{\rm BW}$, the break-up momentum b and the orbital angular momentum L between the final-state particles. The explicit expressions for $L = \{0, 1, 2\}$ are

$$B_0(b) = 1, \quad B_1(b) = 1/\sqrt{1 + (b\,r_{\rm BW})^2} \text{ and } \quad B_2(b) = 1/\sqrt{9 + 3\,(b\,r_{\rm BW})^2 + (b\,r_{\rm BW})^4}. \tag{5}$$

Resonance lineshapes are described by Breit–Wigner propagators,

$$T_R(s) = (m_0^2 - s - i\,\sqrt{s}\,\Gamma(s))^{-1}, \tag{6}$$

where s is the square of the centre-of-mass energy. The energy-dependent decay width, $\Gamma(s)$, is normalised to give the nominal width, Γ_0, when evaluated at the nominal mass, m_0. For a decay into two stable particles $R \to AB$, the energy dependence of the decay width can be described by

$$\sqrt{s}\,\Gamma_{R\to AB}(s) = m_0\,\Gamma_0\,\frac{m_0}{\sqrt{s}}\,\left(\frac{b}{b_0}\right)^{2L+1}\,\frac{B_L(b)^2}{B_L(b_0)^2}\,, \tag{7}$$

where b_0 is the value of the break-up momentum at the resonance pole [24]. Specialised lineshape parameterisations are used for the $f_0(500)^0$ (Bugg [25]), $K_0^*(1430)^0$ (LASS [26,27]) and $\rho(770)^0$ (Gounaris–Sakurai [28]) resonances. The lineshapes for non-resonant states are set to a constant.

The energy-dependent width for a three-body decay $R \to ABC$ is computed by integrating the squared transition amplitude over the phase space,

$$\Gamma_{R\to ABC}(s) = \frac{1}{2\,\sqrt{s}}\,\int |A_{R\to ABC}|^2\,{\rm d}\Phi_3, \tag{8}$$

as described in Ref. [29]. For the $K_1(1270)^+ \to \rho(770)^0 K^+$ cascade decay chain, mixing between the $\rho(770)^0$ and $\omega(782)^0$ states is included [30], with relative magnitude and phase fixed to the values determined in Ref. [31]. More details are given in Appendix A. The spin factors are constructed in the covariant Zemach (Rarita–Schwinger) tensor formalism [32–36]. The explicit expressions for the decay topologies relevant for this analysis are taken from Refs. [29, 37].

2.2 Decay rates

Since B_s^0 mesons can convert into $\overline{B}_s^0$ and vice versa, the flavour eigenstates are an admixture of the physical mass eigenstates B_L and B_H,

$$|B_L\rangle = p|B_s^0\rangle + q|\overline{B}_s^0\rangle, \qquad\qquad |B_H\rangle = p|B_s^0\rangle - q|\overline{B}_s^0\rangle, \tag{9}$$

where the complex coefficients are normalised such that $|p|^2 + |q|^2 = 1$. The light, $|B_L\rangle$, and heavy, $|B_H\rangle$, mass eigenstates have distinct masses, m_L and m_H, and decay widths, Γ_L and Γ_H. Their arithmetic means (differences) are denoted as m_s and Γ_s ($\Delta m_s = m_H - m_L$ and $\Delta\Gamma_s = \Gamma_L - \Gamma_H$). The time evolution of the flavour and mass eigenstates can be described by an effective Schrödinger equation [38,39] resulting in the following differential decay rates for initially produced B_s^0 or $\overline{B}_s^0$ mesons [39–41]:

$$\begin{aligned}
\frac{\mathrm{d}\Gamma(B_s^0 \to f)}{\mathrm{d}t\,\mathrm{d}\Phi_4(\mathbf{x})} = |\langle f|B_s^0(t)\rangle|^2 \propto e^{-\Gamma_s t}\Bigg[&\left(|A^c(\mathbf{x})|^2 + r^2\,|A^u(\mathbf{x})|^2\right)\,\cosh\left(\frac{\Delta\Gamma_s\,t}{2}\right)\\
&+ \left(|A^c(\mathbf{x})|^2 - r^2\,|A^u(\mathbf{x})|^2\right)\,\cos\left(\Delta m_s\,t\right)\\
&- 2\,r\,\mathrm{Re}\left(A^c(\mathbf{x})^*\,A^u(\mathbf{x})\,e^{i(\delta-(\gamma-2\beta_s))}\right)\,\sinh\left(\frac{\Delta\Gamma_s\,t}{2}\right)\\
&- 2\,r\,\mathrm{Im}\left(A^c(\mathbf{x})^*\,A^u(\mathbf{x})\,e^{i(\delta-(\gamma-2\beta_s))}\right)\,\sin\left(\Delta m_s\,t\right)\Bigg],\\
\frac{\mathrm{d}\Gamma(\overline{B}_s^0 \to f)}{\mathrm{d}t\,\mathrm{d}\Phi_4(\mathbf{x})} = |\langle f|\overline{B}_s^0(t)\rangle|^2 \propto e^{-\Gamma_s t}\Bigg[&\left(|A^c(\mathbf{x})|^2 + r^2\,|A^u(\mathbf{x})|^2\right)\,\cosh\left(\frac{\Delta\Gamma_s\,t}{2}\right)\\
&- \left(|A^c(\mathbf{x})|^2 - r^2\,|A^u(\mathbf{x})|^2\right)\,\cos\left(\Delta m_s\,t\right)\\
&- 2\,r\,\mathrm{Re}\left(A^c(\mathbf{x})^*\,A^u(\mathbf{x})\,e^{i(\delta-(\gamma-2\beta_s))}\right)\,\sinh\left(\frac{\Delta\Gamma_s\,t}{2}\right)\\
&+ 2\,r\,\mathrm{Im}\left(A^c(\mathbf{x})^*\,A^u(\mathbf{x})\,e^{i(\delta-(\gamma-2\beta_s))}\right)\,\sin\left(\Delta m_s\,t\right)\Bigg].
\end{aligned} \tag{10}$$

Here, the magnitude of q/p is set to unity (*i.e.* no *CP* violation in mixing is assumed [3, 42]) and the phase between q and p can be related to the mixing phase β_s, $\arg(q/p) \approx -2\beta_s$ [40, 41]. The decay rates to the *CP*-conjugate final state $\bar{f} = D_s^+ K^- \pi^- \pi^+$ (with phase-space point $\overline{\mathbf{x}} \equiv CP\,\mathbf{x}$), $\mathrm{d}\Gamma(\overline{B}_s^0 \to \bar{f})$ and $\mathrm{d}\Gamma(B_s^0 \to \bar{f})$, follow from the expressions for $\mathrm{d}\Gamma(B_s^0 \to f)$ and $\mathrm{d}\Gamma(\overline{B}_s^0 \to f)$ in Eq. (10) by replacing $A^c(\mathbf{x}) \to A^c(\overline{\mathbf{x}})$, $A^u(\mathbf{x}) \to A^u(\overline{\mathbf{x}})$ and $-(\gamma - 2\beta_s) \to +(\gamma - 2\beta_s)$. This assumes no *CP* violation in the hadronic decay amplitudes (*i.e.*, $a_i^c = \bar{a}_i^c$ and $a_i^u = \bar{a}_i^u$), as expected for tree-level-dominated decays.

It is also instructive to examine the decay rates as functions of the decay time only, by marginalising the phase space

$$\begin{aligned}
\frac{\mathrm{d}\Gamma(B_s^0 \to f)}{\mathrm{d}t} \propto \Bigg[&\cosh\left(\frac{\Delta\Gamma_s\,t}{2}\right) + C_f\cos\left(\Delta m_s\,t\right)\\
&+ A_f^{\Delta\Gamma}\sinh\left(\frac{\Delta\Gamma_s\,t}{2}\right) - S_f\sin\left(\Delta m_s\,t\right)\Bigg]e^{-\Gamma_s t},\\
\frac{\mathrm{d}\Gamma(\overline{B}_s^0 \to f)}{\mathrm{d}t} \propto \Bigg[&\cosh\left(\frac{\Delta\Gamma_s\,t}{2}\right) - C_f\cos\left(\Delta m_s\,t\right)\\
&+ A_f^{\Delta\Gamma}\sinh\left(\frac{\Delta\Gamma_s\,t}{2}\right) + S_f\sin\left(\Delta m_s\,t\right)\Bigg]e^{-\Gamma_s t}.
\end{aligned} \tag{11}$$

Analogous expressions for the *CP*-conjugate processes can be written by replacing $A_f^{\Delta\Gamma}$ with $A_{\bar{f}}^{\Delta\Gamma}$ and S_f with $-S_{\bar{f}}$, where the *CP* coefficients are defined as

$$
\begin{aligned}
C_f &= \frac{1-r^2}{1+r^2}, \\
A_f^{\Delta\Gamma} &= -\frac{2\,r\,\kappa\cos\left(\delta-\left(\gamma-2\beta_s\right)\right)}{1+r^2}, \quad A_{\bar{f}}^{\Delta\Gamma} = -\frac{2\,r\,\kappa\cos\left(\delta+\left(\gamma-2\beta_s\right)\right)}{1+r^2}, \\
S_f &= +\frac{2\,r\,\kappa\sin\left(\delta-\left(\gamma-2\beta_s\right)\right)}{1+r^2}, \quad S_{\bar{f}} = -\frac{2\,r\,\kappa\sin\left(\delta+\left(\gamma-2\beta_s\right)\right)}{1+r^2}.
\end{aligned} \tag{12}
$$

The coherence factor, κ, results from the integration over the interfering amplitudes across the phase space, $\kappa \equiv \int A^c(\mathbf{x})^* A^u(\mathbf{x})\,\mathrm{d}\Phi_4$. It is bounded between zero and unity, and dilutes the sensitivity to the weak phase. For the two-body decay $B_s^0 \to D_s^{\mp} K^{\pm}$ the coherence factor is $\kappa = 1$ [17]. Measured values of $A_f^{\Delta\Gamma} \neq A_{\bar{f}}^{\Delta\Gamma}$ or $S_f \neq -S_{\bar{f}}$ signify time-dependent *CP* violation and lead to different mixing asymmetries for decays into the f or $\bar{f}$ final states. These mixing asymmetries are defined as [7, 8]

$$
\begin{aligned}
A_{\mathrm{mix}}^{f}(t) &= \frac{N_f(t)-\bar{N}_f(t)}{N_f(t)+\bar{N}_f(t)} = \frac{C_f\cos\left(\Delta m_s\,t\right) - S_f\sin\left(\Delta m_s\,t\right)}{\cosh\left(\frac{\Delta\Gamma_s\,t}{2}\right) + A_f^{\Delta\Gamma}\sinh\left(\frac{\Delta\Gamma_s\,t}{2}\right)}, \\
A_{\mathrm{mix}}^{\bar{f}}(t) &= \frac{\bar{N}_{\bar{f}}(t)-N_{\bar{f}}(t)}{\bar{N}_{\bar{f}}(t)+N_{\bar{f}}(t)} = \frac{C_f\cos\left(\Delta m_s\,t\right) + S_{\bar{f}}\sin\left(\Delta m_s\,t\right)}{\cosh\left(\frac{\Delta\Gamma_s\,t}{2}\right) + A_{\bar{f}}^{\Delta\Gamma}\sinh\left(\frac{\Delta\Gamma_s\,t}{2}\right)},
\end{aligned} \tag{13}
$$

where $N_f(t)$ ($\bar{N}_f(t)$) and $N_{\bar{f}}(t)$ ($\bar{N}_{\bar{f}}(t)$) denote the number of initially produced B_s^0 ($\overline{B}_s^0$) mesons decaying at proper time t to the final states f and $\bar{f}$, respectively. Flavour-specific decay modes such as $B_s^0 \to D_s^- \pi^+\pi^+\pi^-$ have $r = 0$ and consequently $C_f = 1$ as well as $A_f^{\Delta\Gamma} = A_{\bar{f}}^{\Delta\Gamma} = S_f = S_{\bar{f}} = 0$.

3 Event reconstruction

The LHCb detector [43, 44] is a single-arm forward spectrometer covering the pseudorapidity range $2 < \eta < 5$, designed for the study of particles containing b or c quarks. The detector includes a high-precision tracking system consisting of a silicon-strip vertex detector (VELO) surrounding the pp interaction region [45], a large-area silicon-strip detector located upstream of a dipole magnet with a bending power of about 4 Tm, and three stations of silicon-strip detectors and straw drift tubes [46, 47] placed downstream of the magnet. The polarity of the dipole magnet is reversed periodically throughout the data-taking process to control systematic asymmetries. The tracking system provides a measurement of the momentum, p, of charged particles with a relative uncertainty that varies from 0.5% at low momentum to 1.0% at 200 GeV. The minimum distance of a track to a primary vertex (PV), the impact parameter (IP), is measured with a resolution of $(15+29/p_{\mathrm{T}})\,\mu$m, where p_{T} is the component of the momentum transverse to the beam, in GeV. Different types of charged hadrons are distinguished using information from two ring-imaging Cherenkov detectors [48]. The online event selection is performed by a trigger [49], which consists of a hardware stage, based on information from the calorimeter and muon systems, followed by a software stage, which applies a full event reconstruction. At the hardware trigger stage, events are required to have a muon with high p_{T} or a hadron, photon or electron with high transverse energy in the calorimeters. For hadrons, the transverse energy threshold is 3.5 GeV. The software trigger requires

a two-, three- or four-track secondary vertex with a significant displacement from any primary pp interaction vertex. At least one charged particle must have a transverse momentum $p_{\rm T} > 1.6\,\text{GeV}$ and be inconsistent with originating from a PV. A multivariate algorithm [50] is used for the identification of secondary vertices consistent with the decay of a b hadron. The data-taking period from 2011 to 2012 with centre-of-mass energies of 7 and 8 TeV (2015 to 2018 with centre-of-mass energy of 13 TeV) is referred to as Run 1 (Run 2) throughout the paper.

Simulated events are used to study the detector acceptance and specific background contributions. In the simulation, pp collisions are generated using Pythia [51] with a specific LHCb configuration [52]. Decays of hadrons are described by EvtGen [53], in which final-state radiation is generated using Photos [54]. The simulated signal decays are generated according to a simplified amplitude model with an additional pure phase-space component. The interaction of the generated particles with the detector, and its response, are implemented using the Geant4 toolkit [55] as described in Ref. [56].

3.1 Candidate selection

The selection of $B_s^0 \to D_s^{\mp} K^{\pm}\pi^{\pm}\pi^{\mp}$ and $B_s^0 \to D_s^- \pi^+\pi^+\pi^-$ candidates is performed by first reconstructing $D_s^- \to K^-K^+\pi^-$, $D_s^- \to K^-\pi^-\pi^+$ and $D_s^- \to \pi^-\pi^+\pi^-$ candidates from charged particle tracks with high momentum and transverse momentum originating from a common displaced vertex. Particle identification (PID) information is used to assign a kaon or pion hypothesis to the tracks. Candidate D_s^- mesons with a reconstructed invariant mass within 25 MeV of the known D_s^- mass [2] are combined with three additional charged tracks to form a B_s^0 vertex, which must be displaced from any PV. The PV with respect to which the B_s^0 candidate has the smallest impact parameter significance is considered as the production vertex. The reconstructed invariant mass of the B_s^0 candidate is required to be between 5200 MeV and 5700 MeV. The mass resolution is improved by performing a kinematic fit [57] where the B_s^0 candidate is constrained to originate from the PV and the reconstructed D_s^- mass is constrained to the world-average D_s^- mass [2]. When deriving the decay time, t, of the B_s^0 candidate and the phase-space observables, $\mathbf{x}$, the reconstructed B_s^0 mass is constrained to its known value [2]. The B_s^0 proper time is required to be larger than 0.4 ps to suppress most of the prompt combinatorial background. The considered phase-space region is limited to $m(K^+\pi^+\pi^-) < 1950\,\text{MeV}$, $m(K^+\pi^-) < 1200\,\text{MeV}$ and $m(\pi^+\pi^-) < 1200\,\text{MeV}$ since the decay proceeds predominantly through the low-mass axial-vector states $K_1(1270)^+$ and $K_1(1400)^+$ [58], while the combinatorial background is concentrated at high $K^+\pi^+\pi^-$, $K^+\pi^-$ and $\pi^+\pi^-$ invariant masses. A combination of PID information and kinematic requirements is used to veto charmed meson or baryon decays reconstructed as D_s^- candidates due to the misidentification of protons or pions as kaons.

A boosted decision tree (BDT) [59, 60] with gradient boosting is used to suppress background from random combinations of charged particles. The multivariate classifier is trained using a background-subtracted $B_s^0 \to D_s^- \pi^+\pi^+\pi^-$ data sample as signal proxy, while $B_s^0 \to D_s^{\mp} K^{\pm}\pi^{\pm}\pi^{\mp}$ candidates with invariant mass greater than 5500 MeV are used as background proxy. The features used in the BDT are topological variables related to the vertex separation, such as the impact parameters of the B_s^0 candidate and final-state particles, the flight distance of the D_s^- candidate with respect to the secondary vertex, as well as several criteria on the track quality and vertex reconstruction and estimators of the isolation of the B_s^0 candidate from other tracks in the event. The working point of

the BDT classifier is chosen to optimise the significance of the $B_s^0 \to D_s^\mp K^\pm\pi^\pm\pi^\mp$ signal.

3.2 Data sample composition

Irreducible background contributions to the selected $B_s^0 \to D_s^-\pi^+\pi^+\pi^-$ and $B_s^0 \to D_s^\mp K^\pm\pi^\pm\pi^\mp$ data samples are disentangled from signal decays on a statistical basis by means of an extended maximum likelihood fit to the reconstructed $m(D_s^\mp h^\pm\pi^\pm\pi^\mp)$ invariant mass, where h is either a pion or a kaon. A Johnson's $S_{\rm U}$ function [61] is used as probability density function (PDF) for the signal component. The shape parameters are initially determined from simulation. To account for small differences between simulation and data, scale factors for the mean and standard deviation of the signal PDF are introduced. These are determined from a fit to the $B_s^0 \to D_s^-\pi^+\pi^+\pi^-$ calibration sample and thereafter fixed when fitting $B_s^0 \to D_s^\mp K^\pm\pi^\pm\pi^\mp$ candidates. Background decays of B^0 mesons are described by the same PDF shifted by the known mass difference between B_s^0 and B^0 mesons [2]. The combinatorial background is modelled with a second-order polynomial function. The shapes for partially reconstructed $B_s^0 \to D_s^{*-}\pi^+\pi^+\pi^-$, $B_s^0 \to D_s^{*-}K^+\pi^+\pi^-$ and $B^0 \to D_s^{*-}K^+\pi^+\pi^-$ decays, where the D_s^{*-} meson decays to $D_s^-\gamma$ or $D_s^-\pi^0$, are derived from simulated decays. The same applies to the shape for misidentified $B_s^0 \to D_s^{*-}\pi^+\pi^+\pi^-$ decays contributing to the $B_s^0 \to D_s^\mp K^\pm\pi^\pm\pi^\mp$ sample. The expected yield of this cross-feed background is estimated by determining the probability of a pion to pass the PID requirement imposed on the kaon candidate from a control sample of $D^{*+} \to (D^0 \to K^-\pi^+)\,\pi^+$ decays [62]. All other yields are determined from the fit.

Figure 2 displays the invariant mass distributions of $B_s^0 \to D_s^-\pi^+\pi^+\pi^-$ and $B_s^0 \to D_s^\mp K^\pm\pi^\pm\pi^\mp$ candidates with fit projections overlaid. A signal yield of $148\,000 \pm 400$ (7500 ± 100) is obtained for $B_s^0 \to D_s^-\pi^+\pi^+\pi^-$ ($B_s^0 \to D_s^\mp K^\pm\pi^\pm\pi^\mp$) decays. The results are used to assign weights to the candidates to statistically subtract the background with the *sPlot* technique [63]. Here, the $m(D_s^\mp h^\pm\pi^\pm\pi^\mp)$ invariant mass is used as discriminating variable when performing fits to the decay-time and phase-space distributions [64].

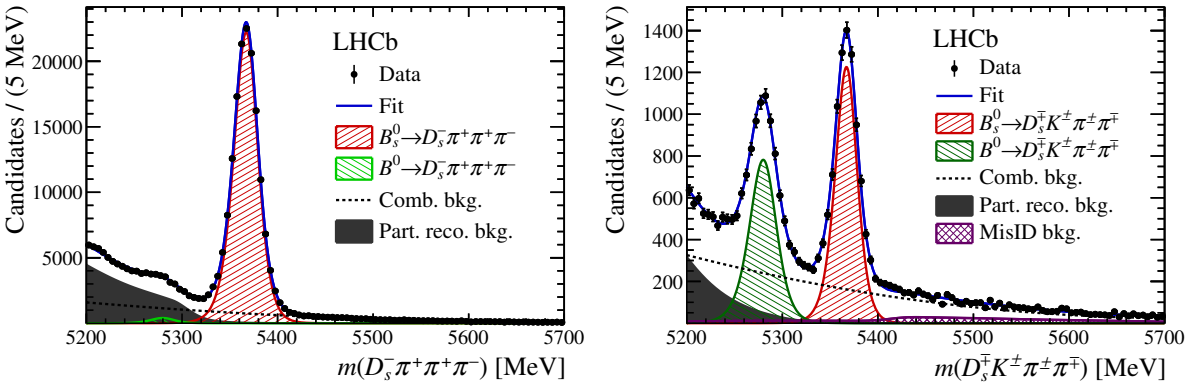

Figure 2: Invariant mass distribution of selected (left) $B_s^0 \to D_s^-\pi^+\pi^+\pi^-$ and (right) $B_s^0 \to D_s^\mp K^\pm\pi^\pm\pi^\mp$ candidates with fit projections overlaid.

4 Measurement of the B_s^0 mixing frequency

A likelihood fit to the background-subtracted decay-time spectrum of the $B_s^0 \to D_s^- \pi^+ \pi^+ \pi^-$ control channel is performed in order to calibrate detector-induced effects and flavour-tagging algorithms as well as to measure the mixing frequency Δm_s.

4.1 Decay-time resolution

Excellent decay-time resolution is essential in order to resolve the fast $B_s^0 - \overline{B}_s^0$ mixing. The global kinematic fit to the decay topology provides an estimate of the decay-time resolution for each candidate. The per-candidate decay-time uncertainty, δ_t, is calibrated by reconstructing B_s^0 candidates from particles originating directly from the PV. These prompt B_s^0 candidates have a known true decay time of zero, such that the width of the decay-time distribution is a measure of the true resolution, σ_t. It is determined in equally populated slices of δ_t. A linear calibration function is used to map the per-candidate decay-time uncertainty to the actual resolution. On average, the resolution amounts to $\langle \sigma_t \rangle = 36.6 \pm 0.5\,\text{fs}$, where the uncertainty is statistical only. A decay-time bias, μ_t, of approximately $-2\,\text{fs}$ is observed which results from the applied selection requirements and the precision of the detector alignment. The implementation of the decay-time bias and decay-time resolution in the fit are discussed in Sec. 4.3.

4.2 Flavour tagging

Two complementary methods are used to determine the flavour of the B_s^0 candidates at production. The opposite-side (OS) tagger [65, 66] exploits the fact that b quarks are predominantly produced in quark-antiquark pairs, which leads to a second b hadron alongside the signal B_s^0 meson. The flavour of the non-signal b hadron is determined using the charge of the lepton (μ, e) produced in semileptonic decays, the charge of a reconstructed secondary charm hadron, the charge of the kaon from the $b \to c \to s$ decay chain, and/or the charge of the inclusive secondary vertex reconstructed from the b hadron decay products. The same-side (SS) tagger [67] determines the flavour of the signal candidate by identifying the charge of the kaon produced together with the B_s^0 meson in the fragmentation process.

Each tagging algorithm provides a flavour-tagging decision, d, which takes the value $d = +1$ ($d = -1$) for a candidate tagged as a B_s^0 ($\overline{B}_s^0$) meson and $d = 0$ if no decision can be made (untagged). The tagging efficiency ϵ_{tag} is defined as the fraction of selected candidates with non-zero tag decision. The tagging algorithms also provide an estimate, η, of the probability that the decision is incorrect. The tagging decision and mistag estimate are obtained using flavour specific, self-tagging, decays. Multivariate classifiers are employed combining various inputs such as kinematic variables of tagging particles and of the signal candidate. These are trained on simulated samples of $B_s^0 \to D_s^- \pi^+$ decays for the SS tagger and on data samples of $B^+ \to J/\psi K^+$ decays for the OS tagger. The mistag estimate does not necessarily represent the true mistag probability, ω, since the algorithms might perform differently on the signal decay than on the decay modes used for the training. Therefore, it is calibrated for each tagger using the flavour-specific decay $B_s^0 \to D_s^- \pi^+ \pi^+ \pi^-$.

4.3 Decay-time fit

The signal PDF describing the $B_s^0 \to D_s^- \pi^+ \pi^+ \pi^-$ proper-time spectrum is based on the theoretical decay rate in Eq. (11) taking several experimental effects into account [16, 17, 68, 69]

$$\begin{aligned}
&\mathcal{P}(t, d_{\rm OS}, d_{\rm SS}, q_f | \delta_t, \eta_{\rm OS}, \eta_{\rm SS}) \propto \\
&\Big[(1 - q_f A_D)\, p(t', d_{\rm OS}, d_{\rm SS}, q_f | \delta_t, \eta_{\rm OS}, \eta_{\rm SS})\, e^{-\Gamma_s t'} \otimes R(t - t' | \mu_t, \sigma_t(\delta_t)) \Big]\, \epsilon(t),
\end{aligned}$$

where

$$\begin{aligned}
&p(t', d_{\rm OS}, d_{\rm SS}, q_f | \delta_t, \eta_{\rm OS}, \eta_{\rm SS}) \equiv \\
&\Bigg[(1 - A_P) h(d_{\rm OS}, \eta_{\rm OS}) h(d_{\rm SS}, \eta_{\rm SS}) \left(\cosh\left(\frac{\Delta\Gamma_s\, t'}{2} \right) + \, q_f \cos\left(\Delta m_s\, t' \right) \right) \\
&+ (1 + A_P) \bar{h}(q_{\rm OS}, \eta_{\rm OS}) \bar{h}(d_{\rm SS}, \eta_{\rm SS}) \left(\cosh\left(\frac{\Delta\Gamma_s\, t'}{2} \right) - \, q_f \cos\left(\Delta m_s\, t' \right) \right) \Bigg], \\
&h(d, \eta) \equiv |d| \left[1 + d \left(1 - 2\, w(\eta) \right) \right] \epsilon_{\rm tag} + 2\, (1 - |d|)\, (1 - \epsilon_{\rm tag}), \\
&\bar{h}(d, \eta) \equiv |d| \left[1 - d \left(1 - 2\, \bar{w}(\eta) \right) \right] \bar{\epsilon}_{\rm tag} + 2\, (1 - |d|)\, (1 - \bar{\epsilon}_{\rm tag}).
\end{aligned} \tag{14}$$

This PDF depends on the tagging decisions of the OS and SS taggers, $d_{\rm OS}$ and $d_{\rm SS}$; on the final state, $q_f = +1(-1)$ for $f = D_s^- \pi^+ \pi^+ \pi^- (\bar{f} = D_s^+ \pi^- \pi^- \pi^+)$; and is conditional on the per-event observables [70] $\delta_t, \eta_{\rm OS}$ and $\eta_{\rm SS}$, describing the estimated decay-time error and the estimated mistag rates of the OS and SS taggers, respectively. The parameters of the Gaussian resolution model, $R(t - t' | \mu_t, \sigma_t(\delta_t))$, are fixed to the values determined from the prompt candidate data sample. The decay-time-dependent efficiency, $\epsilon(t)$, of reconstructing and selecting signal decays is modelled by a B-spline curve [71, 72], whose cubic polynomials are uniquely defined by a set of knots. These are placed across the considered decay-time range to account for local variations [73]. Six knots are chosen such that there is an approximately equal amount of data in-between two consecutive knots. By fixing the decay width $\Gamma_s = (0.6624 \pm 0.0018)$ ps^{-1} and decay width difference $\Delta\Gamma_s = (0.090 \pm 0.005)$ ps^{-1} to their world-average values [3], the spline coefficients can be directly determined in the fit to the data. The correlation $\rho(\Gamma_s, \Delta\Gamma_s) = -0.080$ is taken into account when evaluating the systematic uncertainties.

Both taggers are simultaneously calibrated during the fit as described by the functions $h(d, \eta)$ and $\bar{h}(d, \eta)$. These also take into account a small dependence of the tagging performance on the initial B_s^0 flavour by introducing linear calibration functions for initial B_s^0 and $\overline{B}_s^0$ mesons denoted as $\omega(\eta)$ and $\bar{\omega}(\eta)$, respectively. Similarly, $\epsilon_{\rm tag}$ ($\bar{\epsilon}_{\rm tag}$) denotes the tagging efficiency for an initial B_s^0 ($\overline{B}_s^0$) meson. The calibrated responses of the OS and SS taggers are then explicitly combined in the PDF. Since the tagging algorithms have been retuned for the Run 2 data-taking period [74] to account for the changed conditions, separate calibrations for the two data-taking periods are performed.

The production asymmetries between B_s^0 and $\overline{B}_s^0$ mesons at centre-of-mass energies of

7 TeV and 8 TeV are taken from an LHCb measurement using $B_s^0 \to D_s^- \pi^+$ decays [75]. After correcting for kinematic differences between $B_s^0 \to D_s^- \pi^+$ and $B_s^0 \to D_s^- \pi^+ \pi^+ \pi^-$ decays, the effective production asymmetry, $A_P = (N(\overline{B}_s^0) - N(B_s^0))/(N(\overline{B}_s^0) + N(B_s^0))$, for Run 1 data amounts to $A_P = (-0.1 \pm 1.0)\%$. The production asymmetry at a centre-of-mass energy of 13 TeV is determined in the fit. A detection asymmetry between the final states is caused by the different interaction cross-sections of positively and negatively charged kaons with the detector material. The detection asymmetry is defined as $A_D = (\varepsilon(\bar{f}) - \varepsilon(f))/(\varepsilon(\bar{f}) + \varepsilon(f))$, where $\varepsilon(\bar{f})$ ($\varepsilon(f)$) denotes the detection efficiency of final state $\bar{f}$ (f). It is computed by comparing the charge asymmetries in $D^\pm \to K^\mp \pi^\pm \pi^\pm$ and $D^\pm \to K_S^0 \pi^\pm$ calibration samples [76], weighted to match the kinematics of the signal kaon. Only the decay mode $D_s^- \to K^- \pi^- \pi^+$ is a possible source of detection asymmetry for $B_s^0 \to D_s^- \pi^+ \pi^+ \pi^-$ decays resulting in an average detection asymmetry of $A_D = (-0.07 \pm 0.15)\%$ for Run 1 and $A_D = (-0.08 \pm 0.21)\%$ for Run 2 data. A sufficiently large subsample of the Run 2 data set is used to reconstruct the calibration modes for this study.

Figure 3 displays the decay-time distribution and the mixing asymmetry for $B_s^0 \to D_s^- \pi^+ \pi^+ \pi^-$ signal candidates. The latter is weighted by the per-candidate time resolution and flavour-tagging dilution to enhance the visible asymmetry. All features are well reproduced by the fit projections which are overlaid. The $B_s^0 - \overline{B}_s^0$ mixing frequency

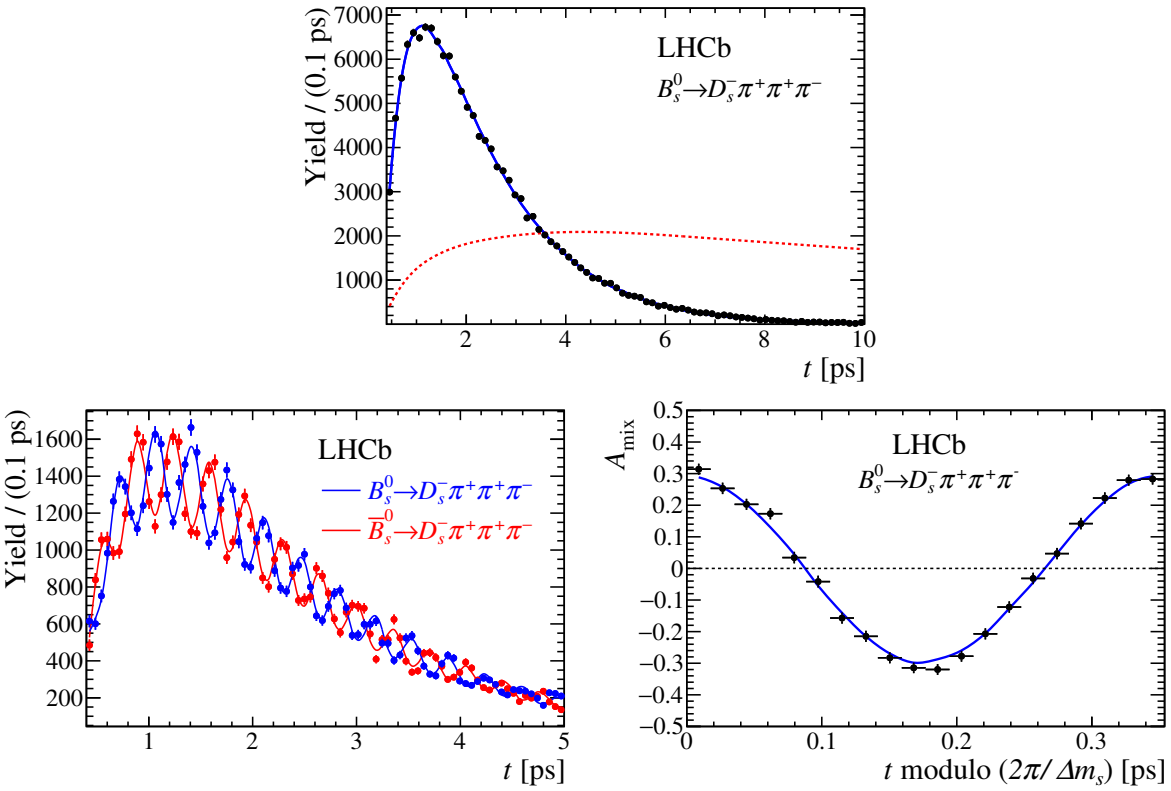

Figure 3: Background-subtracted decay-time distribution of (top) all and (bottom left) tagged $B_s^0 \to D_s^- \pi^+ \pi^+ \pi^-$ candidates as well as (bottom right) the dilution-weighted mixing asymmetry folded into one oscillation period along with the fit projections (solid lines). The decay-time acceptance (top) is overlaid in an arbitrary scale (dashed line).

Table 1: The flavour-tagging performance for only OS-tagged, only SS-tagged and both OS- and SS-tagged $B_s^0 \to D_s^- \pi^+ \pi^+ \pi^-$ signal candidates.

(a) Run 1 data.

	$\epsilon_{\text{tag}}[\%]$	$\langle\omega\rangle[\%]$	$\epsilon_{\text{eff}}[\%]$
Only OS	14.74 ± 0.11	39.09 ± 0.80	1.25 ± 0.16
Only SS	35.38 ± 0.18	44.26 ± 0.62	1.05 ± 0.18
Both OS-SS	33.04 ± 0.30	37.33 ± 0.73	3.41 ± 0.33
Combined	83.16 ± 0.37	40.59 ± 0.70	5.71 ± 0.40

(b) Run 2 data.

	$\epsilon_{\text{tag}}[\%]$	$\langle\omega\rangle[\%]$	$\epsilon_{\text{eff}}[\%]$
Only OS	11.91 ± 0.04	37.33 ± 0.41	1.11 ± 0.05
Only SS	40.95 ± 0.08	42.41 ± 0.29	1.81 ± 0.10
Both OS-SS	28.96 ± 0.12	35.51 ± 0.32	3.61 ± 0.13
Combined	81.82 ± 0.15	39.23 ± 0.32	6.52 ± 0.17

is determined to be

$$\Delta m_s = (17.757 \pm 0.007 \pm 0.008)\,\text{ps}^{-1},$$

where the first uncertainty is statistical and the second systematic. The systematic studies are discussed in Sec. 6. Within uncertainties, the measured production asymmetry for Run 2 data, $A_P = (0.1 \pm 0.5 \pm 0.1)\%$, is consistent with zero. The calibrated per-candidate mistag probabilities, ω_i, are used to compute the effective tagging power as $\epsilon_{\text{eff}} = \frac{1}{N}\sum_i (1-2\omega_i)^2$, where N is the total number of signal candidates and a value of $\omega_i = 0.5$ is assigned to untagged candidates. Table 1 reports the observed tagging performance for Run 1 and Run 2 data considering three mutually exclusive categories: tagged by the OS combination algorithm only, tagged by the SS kaon algorithm only and tagged by both OS and SS algorithms. While the flavour taggers suffer from the higher track multiplicity during the Run 2 data-taking period, they profit from the harder momentum spectrum of the produced $b\bar{b}$ quark pair. Combined, this results in a net relative improvement of 14% in effective tagging power.

5 Measurement of the CKM angle γ

This section first describes the phase-space-integrated decay-time analysis of the signal channel $B_s^0 \to D_s^\mp K^\pm \pi^\pm \pi^\mp$ that allows the determination of the CKM angle γ in a model-independent way. Afterwards, the resonance spectrum in $B_s^0 \to D_s^\mp K^\pm \pi^\pm \pi^\mp$ decays is studied and a full time-dependent amplitude analysis is performed for a model-dependent determination of the CKM angle γ.

5.1 Model-independent analysis

The decay-time fit to the $B_s^0 \to D_s^\mp K^\pm \pi^\pm \pi^\mp$ candidates uses a signal PDF based on Eq. (11) with modifications accounting for the experimental effects described in Sec. 4.3. The B_s^0 production asymmetry for Run 2 data and the $B_s^0 - \overline{B}_s^0$ mixing frequency are fixed to the

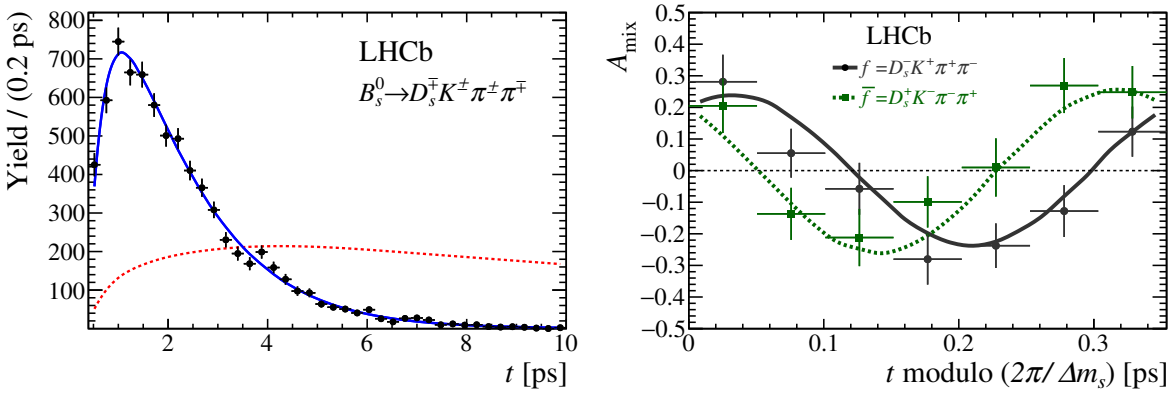

Figure 4: Decay-time distribution of (left) background-subtracted $B_s^0 \to D_s^\mp K^\pm \pi^\pm \pi^\mp$ candidates and (right) dilution-weighted mixing asymmetry along with the model-independent fit projections (solid lines). The decay-time acceptance (left) is overlaid in an arbitrary scale (dashed line).

Table 2: *CP* coefficients determined from the phase-space fit to the $B_s^0 \to D_s^\mp K^\pm \pi^\pm \pi^\mp$ decay-time distribution. The uncertainties are statistical and systematic (discussed in Sec. 6).

Fit parameter	Value
C_f	$0.631 \pm 0.096 \pm 0.032$
$A_f^{\Delta\Gamma}$	$-0.334 \pm 0.232 \pm 0.097$
$A_{\bar{f}}^{\Delta\Gamma}$	$-0.695 \pm 0.215 \pm 0.081$
S_f	$-0.424 \pm 0.135 \pm 0.033$
$S_{\bar{f}}$	$-0.463 \pm 0.134 \pm 0.031$

values obtained from the $B_s^0 \to D_s^- \pi^+ \pi^+ \pi^-$ data sample, whereas the tagging calibration parameters are allowed to vary within Gaussian constraints. The kaon detection asymmetry for $B_s^0 \to D_s^\mp K^\pm \pi^\pm \pi^\mp$ decays is determined in a similar manner as for $B_s^0 \to D_s^- \pi^+ \pi^+ \pi^-$ decays and amounts to $A_D = (-1.02 \pm 0.15)\%$ for Run 1 and $A_D = (-0.91 \pm 0.22)\%$ for Run 2 data. The decay-time acceptance is also fixed to the $B_s^0 \to D_s^- \pi^+ \pi^+ \pi^-$ result, corrected by a decay-time dependent correction factor derived from simulation to account for small differences in the selection and decay kinematics between the decay modes. Otherwise, the fit strategy is identical to that discussed in the previous section. Figure 4 shows the decay-time distribution and mixing asymmetries together with the fit projections. The mixing asymmetries for $D_s^- K^+ \pi^+ \pi^-$ and $D_s^+ K^- \pi^- \pi^+$ final states are shifted with respect to each other indicating mixing-induced *CP* violation, *cf.* Eq. (13). The *CP* coefficients C_f, $A_f^{\Delta\Gamma}$, $A_{\bar{f}}^{\Delta\Gamma}$, S_f and $S_{\bar{f}}$ determined from the fit are reported in Table 2. They are converted to the parameters of interest r, κ, δ and $\gamma - 2\beta_s$ in Sec. 7.

5.2 Time-dependent amplitude analysis

To perform the time-dependent amplitude fit, a signal PDF is employed which replaces the phase-space integrated decay rate with the full decay rate given in Eq. (10), but is otherwise identical to the PDF used in Sec. 5.1. Variations of the selection efficiency over

the phase space are incorporated by evaluating the likelihood normalisation integrals with the Monte Carlo (MC) integration technique using fully simulated decays [29, 77–79].

The light meson spectrum comprises a large number of resonances potentially contributing to the $B_s^0 \to D_s^\mp K^\pm \pi^\pm \pi^\mp$ decay in various decay topologies and angular momentum configurations. The full list of considered intermediate-state amplitudes can be found in Table B.1. A significant complication arises from the fact that two (quasi-independent) amplitude models need to be developed simultaneously: one amplitude describes decays via $b \to c$ ($A^c(\mathbf{x})$), the other decays via $b \to u$ ($A^u(\mathbf{x})$) quark-level transitions. A model building procedure is applied to obtain a good description of the observed phase-space distribution while keeping the number of included amplitudes as small as possible. This is accomplished in two stages. The first stage identifies the set of intermediate-state amplitudes contributing at a significant level to either decays via $b \to c$ or $b \to u$ quark-level transitions or to both. To that end, the time-integrated and flavour-averaged phase-space distribution is examined. A single total amplitude, $A^{\text{eff}}(\mathbf{x}) = \sum_i a_i^{\text{eff}} A_i(\mathbf{x})$, is sufficient in this case, which effectively describes the incoherent superposition of the $b \to c$ and $b \to u$ amplitudes, $|A^{\text{eff}}(\mathbf{x})|^2 = |A^c(\mathbf{x})|^2 + r^2\,|A^u(\mathbf{x})|^2$. This significantly simplified fitting procedure allows the initial inclusion of the whole pool of considered intermediate-state amplitudes, limiting the model complexity with the LASSO technique [29, 80, 81]. This method adds a penalty term to the likelihood function,

$$-2\,\log\mathcal{L} \to -2\,\log\mathcal{L} + \lambda \sum_i \sqrt{\int |a_i^{\text{eff}} A_i(\mathbf{x})|^2\,\mathrm{d}\Phi_4}, \tag{15}$$

which shrinks the amplitude coefficients towards zero. The optimal value for the LASSO parameter λ, which controls the model complexity, is found by minimising the Bayesian information criterion $\text{BIC}(\lambda) = -2\,\log\mathcal{L} + k\,\log N_{\text{Sig}}$ [82], where N_{Sig} is the signal yield and k is the number of amplitudes with a decay fraction above the threshold of 0.5%. The amplitudes with a decay fraction above the threshold at the minimum $\text{BIC}(\lambda)$ value are selected. The second stage of the model selection performs a full time-dependent amplitude fit. The components selected by the first stage are included for both $b \to c$ and $b \to u$ transitions and a LASSO penalty term for each is added to the likelihood function. As the strong interaction is *CP* symmetric, the subdecay modes of three-body resonances and their conjugates are constrained to be the same. The final set of $b \to c$ and $b \to u$ amplitudes is henceforth referred to as the baseline model. The LASSO penalty term is only used to select the model and discarded in the final fit to avoid biasing the parameter uncertainties.

Table B.2 and B.3 list the moduli and phases of the complex amplitude coefficients obtained by fitting the baseline model to the background-subtracted $B_s^0 \to D_s^\mp K^\pm \pi^\pm \pi^\mp$ signal candidates. The corresponding decay fractions for the $b \to c$ and $b \to u$ amplitudes are given in Table 3. The decay-time projection and mixing asymmetries shown in Fig. 5 are consistent with those of the phase-space integrated fit in Fig. 4. Invariant-mass projections are shown in Figs. 6 and 7 indicating that the model provides a reasonable description of the data. Decays via $b \to c$ quark-level transitions are found to be dominated by the axial-vector states $K_1(1270)^+$ and $K_1(1400)^+$. These resonances are produced by the external weak current (see Fig. 1). The sub-leading contribution comes from the vector resonance $K^*(1410)^+$. In $b \to u$ quark-level transitions, the excited kaon states are produced by the spectator-quark interaction. Here, no clear hierarchy is observed. There are sizeable contributions from the axial-vector resonances but also from the pseudoscalar state $K(1460)^+$ and

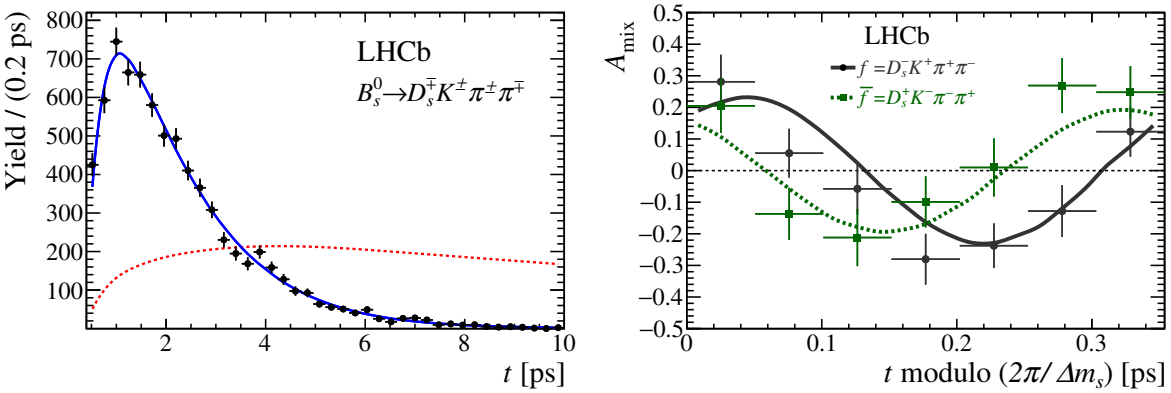

Figure 5: Decay-time distribution of (left) background-subtracted $B_s^0 \to D_s^\mp K^\pm \pi^\pm \pi^\mp$ candidates and (right) dilution-weighted mixing asymmetry along with the model-dependent fit projections (solid lines). The decay-time acceptance (left) is overlaid in an arbitrary scale (dashed line).

Table 3: Decay fractions of the intermediate-state amplitudes contributing to decays via $b \to c$ and $b \to u$ quark-level transitions. The uncertainties are statistical, systematic and due to alternative amplitude models considered.

Decay channel	F_i^c[%]	F_i^u[%]
$B_s^0 \to D_s^\mp\,(K_1(1270)^\pm \to K^*(892)^0\,\pi^\pm)$	$13.0 \pm 2.4 \pm 2.7 \pm 3.4$	$4.1 \pm 2.2 \pm 2.9 \pm 2.6$
$B_s^0 \to D_s^\mp\,(K_1(1270)^\pm \to K^\pm\,\rho(770)^0)$	$16.0 \pm 1.4 \pm 1.8 \pm 2.1$	$5.1 \pm 2.2 \pm 3.5 \pm 2.0$
$B_s^0 \to D_s^\mp\,(K_1(1270)^\pm \to K_0^*(1430)^0\,\pi^\pm)$	$3.4 \pm 0.5 \pm 1.0 \pm 0.4$	$1.1 \pm 0.5 \pm 0.6 \pm 0.5$
$B_s^0 \to D_s^\mp\,(K_1(1400)^\pm \to K^*(892)^0\,\pi^\pm)$	$63.9 \pm 5.1 \pm 7.4 \pm 13.5$	$19.3 \pm 5.2 \pm 8.3 \pm 7.8$
$B_s^0 \to D_s^\mp\,(K^*(1410)^\pm \to K^*(892)^0\,\pi^\pm)$	$12.8 \pm 0.8 \pm 1.5 \pm 3.2$	$12.6 \pm 2.0 \pm 2.6 \pm 4.1$
$B_s^0 \to D_s^\mp\,(K^*(1410)^\pm \to K^\pm\,\rho(770)^0)$	$5.6 \pm 0.4 \pm 0.6 \pm 0.7$	$5.6 \pm 1.0 \pm 1.2 \pm 1.8$
$B_s^0 \to D_s^\mp\,(K(1460)^\pm \to K^*(892)^0\,\pi^\pm)$		$11.9 \pm 2.5 \pm 2.9 \pm 3.1$
$B_s^0 \to (D_s^\mp\,\pi^\pm)_P\ K^*(892)^0$	$10.2 \pm 1.6 \pm 1.8 \pm 4.5$	$28.4 \pm 5.6 \pm 6.4 \pm 15.3$
$B_s^0 \to (D_s^\mp\,K^\pm)_P\ \rho(770)^0$	$0.9 \pm 0.4 \pm 0.5 \pm 1.0$	
Sum	$125.7 \pm 6.4 \pm 6.9 \pm 19.9$	$88.1 \pm 7.0 \pm 10.0 \pm 20.9$

from the quasi-two-body process $B_s^0 \to (D_s^\mp\,\pi^\pm)_P\ K^*(892)^0$, where $(D_s^\mp\,\pi^\pm)_P$ denotes a non-resonant two-particle system in a P-wave ($L = 1$) configuration. Interference fractions of the $b \to c$ and $b \to u$ intermediate-state amplitudes are given in Tables B.6 and B.7. Sizeable interference effects between the decay modes $B_s^0 \to D_s^\mp\,(K_1(1270)^\pm \to K^*(892)^0\,\pi^\pm)$, $B_s^0 \to D_s^\mp\,(K_1(1400)^\pm \to K^*(892)^0\,\pi^\pm)$ and $B_s^0 \to (D_s^\mp\,\pi^\pm)_P\ K^*(892)^0$ are observed since the overlap of their phase-space distributions is significant. A net constructive (destructive) interference effect of all amplitude components of around +26% (−36%) remains for $b \to c$ ($b \to u$) quark-level transitions when integrated over the phase space.

The mass and width of the $K_1(1400)^+$ and $K^*(1410)^+$ resonances are determined from the fit to be

$$m_{K_1(1400)} = (1406 \pm 7 \pm 6 \pm 11)\,\text{MeV}, \qquad \Gamma_{K_1(1400)} = (195 \pm 11 \pm 12 \pm 16)\,\text{MeV},$$
$$m_{K^*(1410)} = (1433 \pm 10 \pm 23 \pm 8)\,\text{MeV}, \qquad \Gamma_{K^*(1410)} = (402 \pm 24 \pm 47 \pm 22)\,\text{MeV},$$

in good agreement with the PDG average values [2]. The uncertainties are statistical, systematic and due to alternative models considered as detailed in Sec. 6. The ratio of

the $B_s^0 \to D_s^- K^+\pi^+\pi^-$ and $\bar{B}_s^0 \to D_s^- K^+\pi^+\pi^-$ decay amplitudes as well as their strong- and weak-phase difference are measured to be

$$\begin{aligned} r &= 0.56 \pm 0.05 \pm 0.04 \pm 0.07, \\ \delta &= (-14 \pm 10 \pm 4 \pm 5)^\circ, \\ \gamma - 2\beta_s &= (\ \ 42 \pm 10 \pm 4 \pm 5)^\circ, \end{aligned}$$

where the angles are given modulo 180°. The coherence factor is computed by numerically integrating over the phase space using the baseline model resulting in

$$\kappa = 0.72 \pm 0.04\,(\text{stat}) \pm 0.06\,(\text{syst}) \pm 0.04\,(\text{model}).$$

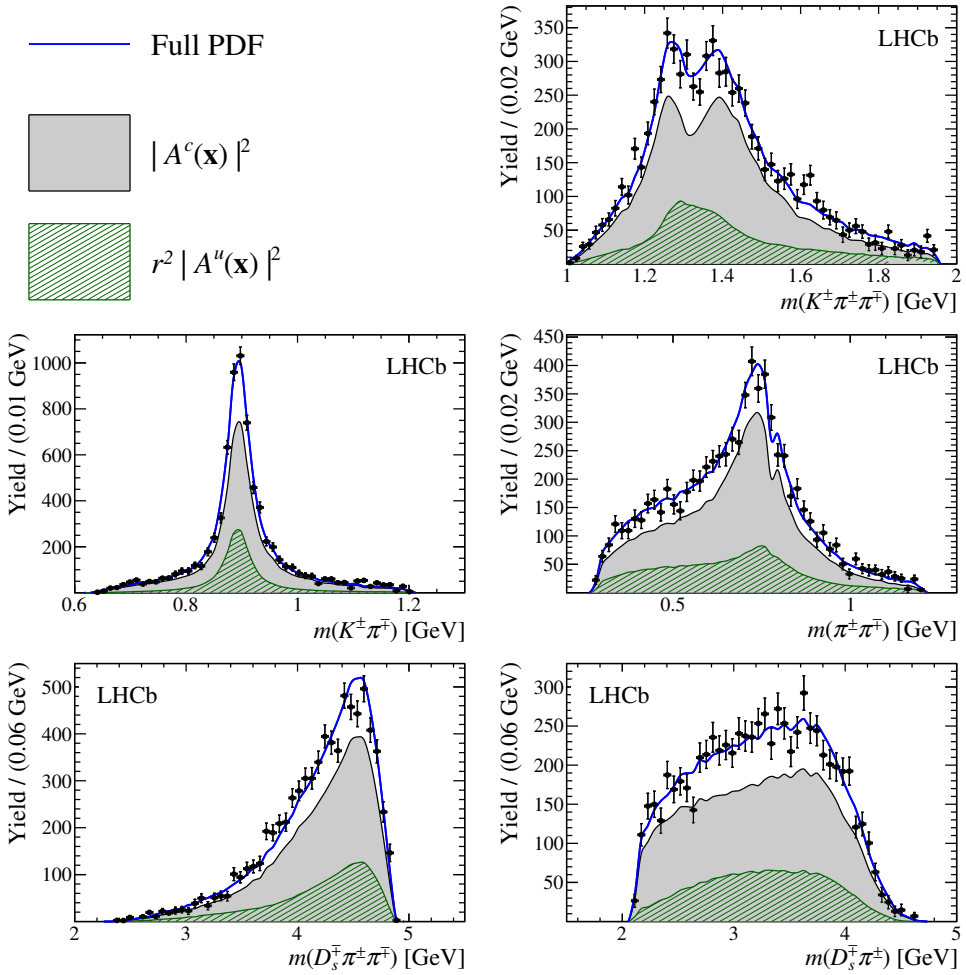

Figure 6: Invariant-mass distribution of background-subtracted $B_s^0 \to D_s^\mp K^\pm\pi^\pm\pi^\mp$ candidates (data points) and fit projections (blue solid line). Contributions from $b \to c$ and $b \to u$ decay amplitudes are overlaid.

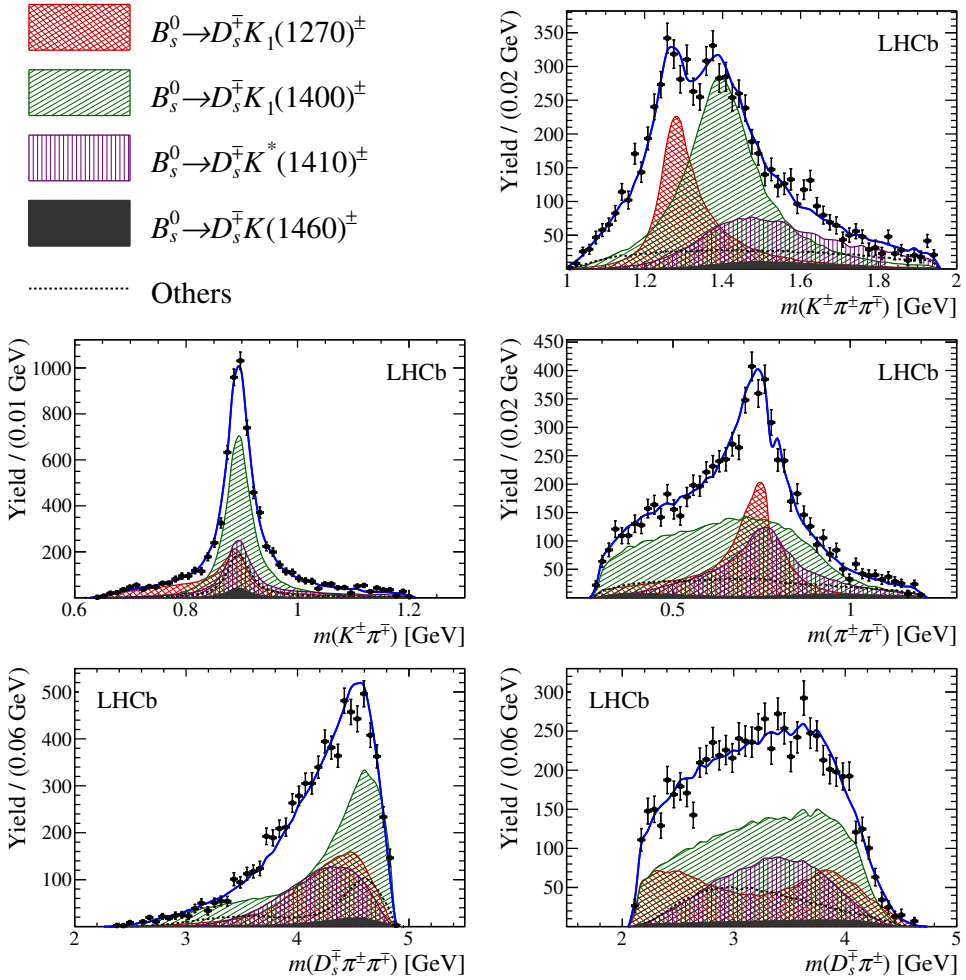

Figure 7: Invariant-mass distribution of background-subtracted $B_s^0 \to D_s^\mp K^\pm\pi^\pm\pi^\mp$ candidates (data points) and fit projections (blue solid line). Incoherent contributions from intermediate-state components are overlaid.

6 Systematic uncertainties

The systematic uncertainties on the measured observables are summarised in Table 4 for the decay-time fits to $B_s^0 \to D_s^-\pi^+\pi^+\pi^-$ and $B_s^0 \to D_s^\mp K^\pm\pi^\pm\pi^\mp$ decays and in Tables 5 and B.4 for the time-dependent amplitude fit to $B_s^0 \to D_s^\mp K^\pm\pi^\pm\pi^\mp$ decays. The various sources of systematic uncertainties are described in the following.

The overall fit procedure is tested by generating pseudoexperiments from the default fit model using the measured values and subsequently fitting them with the same model. For each pseudoexperiment and fit parameter, a pull is calculated by dividing the difference between the fitted and generated values by the statistical uncertainty. The means of the pull distributions are assigned as systematic uncertainties due to an intrinsic fit bias. A closure test using a large sample of fully simulated signal candidates shows a non-significant bias for the determination of Δm_s, which is assigned as a systematic uncertainty.

The statistical subtraction of the residual background relies on the correct description of the reconstructed $m(D_s^\mp h^\pm\pi^\pm\pi^\mp)$ invariant mass distribution. Alternative parameterisa-

Table 4: Systematic uncertainties on the B_s^0 mixing frequency determined from the fit to $B_s^0 \to D_s^- \pi^+ \pi^+ \pi^-$ signal candidates and on the fit parameters of the phase-space integrated fit to $B_s^0 \to D_s^\mp K^\pm \pi^\pm \pi^\mp$ signal candidates in units of the statistical standard deviations.

Systematic	Δm_s	C_f	$A_f^{\Delta\Gamma}$	$A_{\bar{f}}^{\Delta\Gamma}$	S_f	$S_{\bar{f}}$
Fit bias (+ closure test)	0.39	0.09	0.00	0.01	0.02	0.11
Background subtraction	0.18	0.17	0.19	0.18	0.11	0.06
Correlations	0.09	0.11	0.32	0.24	0.04	0.06
Acceptance	0.02	0.03	0.19	0.22	0.02	0.02
Resolution	0.16	0.24	0.01	0.03	0.12	0.10
Decay-time bias	1.00	0.06	0.00	0.00	0.10	0.08
Nuisance asymmetries	0.02	0.06	0.06	0.06	0.06	0.05
VELO z scale	0.26					
VELO alignment	0.44					
Δm_s		0.02	0.01	0.01	0.12	0.12
Total	1.21	0.34	0.42	0.38	0.24	0.23

tions are tested for the signal and each background component. The yields of the cross-feed contributions to the $B_s^0 \to D_s^\mp K^\pm \pi^\pm \pi^\mp$ candidates estimated from a combination of simulated data and control modes are fixed to zero or doubled. The standard deviations of the obtained differences to the default fit values are assigned as a systematic uncertainty due to the background subtraction. The background subtraction technique relies on the assumption of independence between the reconstructed $m(D_s^\mp h^\pm \pi^\pm \pi^\mp)$ invariant mass and the observables that are used in the final fit. The impact of ignoring the small correlation between reconstructed mass and decay time observed for the combinatorial background is determined with pseudoexperiments in which the correlation is included at generation and neglected in the fit.

The systematic uncertainties related to the decay-time acceptance as well as due to the limited experimental knowledge of Γ_s and $\Delta\Gamma_s$ are studied simultaneously. Pseudoexperiments are generated assuming the default configuration and subsequently fitted under both this default and an alternative configuration in which the acceptance parameters together with Γ_s and $\Delta\Gamma_s$ are randomised within their uncertainties (taking their correlation into account). The bias of the mean of the resulting pull distribution is added in quadrature to the pull width in order to arrive at the final systematic uncertainty.

Systematic effects originating from the calibration of the decay-time uncertainty estimate are studied with two alternative parameterisations which either slightly overestimate or underestimate the decay-time resolution. Due to the high correlation between the decay-time resolution and the calibration of the flavour taggers, their systematic uncertainty is studied simultaneously. As a first step, the decay-time fit to the $B_s^0 \to D_s^- \pi^+ \pi^+ \pi^-$ candidates is repeated using the alternative decay-time error calibration functions. New tagging calibration parameters are obtained which are then used (together with the respective decay-time error calibration function) for the fits to the $B_s^0 \to D_s^\mp K^\pm \pi^\pm \pi^\mp$ candidates. The largest deviations of the central values from their default values are assigned as a systematic uncertainty for each fit parameter. A systematic uncertainty due to the limited knowledge of the decay-time bias which is fixed in the fit is evaluated by

Table 5: Systematic uncertainties on the physical observables and resonance parameters determined from the full time-dependent amplitude fit to $B_s^0 \to D_s^{\mp} K^{\pm}\pi^{\pm}\pi^{\mp}$ data in units of the statistical standard deviations. The systematic uncertainties for the amplitude coefficients are given in Table B.4.

Systematic	$m_{K_1(1400)}$	$\Gamma_{K_1(1400)}$	$m_{K^*(1410)}$	$\Gamma_{K^*(1410)}$	r	δ	$\gamma - 2\beta_s$
Fit bias	0.00	0.14	0.14	0.42	0.06	0.13	0.13
Background subtraction	0.15	0.28	0.15	0.41	0.15	0.15	0.22
Correlations	0.23	0.27	0.18	0.07	0.13	0.05	0.08
Time acceptance	0.01	0.01	0.00	0.00	0.06	0.04	0.07
Resolution	0.11	0.33	0.09	0.03	0.30	0.27	0.26
Decay-time bias	0.00	0.02	0.01	0.00	0.02	0.12	0.01
Nuisance asymmetries	0.00	0.01	0.00	0.00	0.01	0.07	0.03
Δm_s	0.00	0.01	0.00	0.00	0.03	0.06	0.03
Phase-space acceptance	0.17	0.34	0.32	0.21	0.35	0.08	0.06
Acceptance factorisation	0.25	0.41	0.76	0.36	0.49	0.08	0.05
Lineshapes	0.52	0.53	0.43	0.29	0.34	0.14	0.13
Resonances m, Γ	0.07	0.06	0.02	0.02	0.02	0.01	0.01
Form factors	0.51	0.60	2.03	1.74	0.12	0.13	0.07
Amplitude model	1.59	1.50	0.77	0.88	1.60	0.51	0.47
Total	1.80	1.86	2.38	2.10	1.79	0.67	0.63

randomising the value within its uncertainty.

The systematic uncertainty from the production and detection asymmetries and Δm_s (in case of $B_s^0 \to D_s^{\mp} K^{\pm}\pi^{\pm}\pi^{\mp}$ decays) which are fixed in the fit are evaluated by means of pseudoexperiments, analogously to the procedure performed for the decay-time acceptance.

The precision with which the B_s^0 flight distance can be determined is limited by the knowledge of the overall length of the VELO detector (VELO z scale) and the position of the individual VELO modules (VELO alignment). This VELO-reconstruction uncertainty translates into a relative uncertainty on Δm_s of 0.02% [68] with other parameters being unaffected. In the fit to the $B_s^0 \to D_s^{\mp} K^{\pm}\pi^{\pm}\pi^{\mp}$ candidates, the VELO-reconstruction uncertainty is then implicitly included in the systematic error due to the Δm_s uncertainty described above.

The treatment of the phase-space acceptance relies on simulated data. The integration error due to the limited size of the simulated sample used to normalise the signal PDF is below 0.2% and thus negligibly small. To assess the uncertainty due to possible data-simulation differences, alternative phase-space acceptances are derived by varying the selection requirements (for the simulated sample only) on quantities that are expected not to be well described by the simulation. It is assumed that the phase-space acceptance is independent of the decay time. This assumption is tested by using only simulated candidates within specific decay-time intervals to calculate the MC normalisation integrals. Four approximately equally populated decay-time intervals are chosen and the sample variance of the fitted values is assigned as a systematic uncertainty.

The lineshape parameterisations for the $\rho(770)^0$ and $K_0^*(1430)^0$ resonances are replaced

by a relativistic Breit–Wigner propagator given by Eq. (7) as part of the systematic studies. Moreover, energy-dependent decay widths of three-body resonances are recomputed taking only the dominant $K^{\pm}\pi^{\pm}\pi^{\mp}$ decay mode into account. For each alteration, a time-dependent amplitude fit is performed and the standard deviation of the obtained fit results is assigned as a systematic uncertainty. Systematic uncertainties due to fixed resonance masses and widths are computed with the same procedure used for the other fixed parameters mentioned above. Similarly, pseudoexperiments are performed in which the Blatt–Weisskopf radial parameter r_{BW} (set to $1.5\,\mathrm{GeV}^{-1}$ by default) is varied uniformly within the interval $[0, 3]\,\mathrm{GeV}^{-1}$ to assign a systematic uncertainty due to the form-factor modelling.

Several modifications to the baseline model are tested to assign an additional uncertainty due to the choice of amplitude components: all amplitudes selected by the first stage of the model selection are included for both $b \to c$ and $b \to u$ transitions, the amplitudes with the smallest decay fraction are removed, additional sub-decay modes of selected three-body resonances are considered, higher orbital angular momentum states are included where applicable, the orbital angular momentum state of non-resonant two-body states is set to other allowed values, additional cascade and quasi-two-body amplitudes (which were removed by the first stage of the model selection) are considered. In total, twelve amplitude models with similar fit quality as the baseline model are identified. The fit results for those are summarised in Tables B.8 and B.9. The largest deviations from the baseline values for r, δ and $\gamma - 2\beta$ are $0.19, 10^{\circ}$ and 12° observed for alternative models 8, 1 and 11, respectively. The standard deviation of the twelve fit results is taken as the model uncertainty. No model uncertainty is assigned to the amplitude coefficients since they are, by definition, parameters of a given model.

7 Results

To interpret the parameters determined in the model-independent fit, $P_{\mathrm{obs}} \equiv (C_f, A_f^{\Delta\Gamma}, A_{\bar{f}}^{\Delta\Gamma}, S_f, S_{\bar{f}})$, in terms of the physical observables $\Lambda \equiv (r, \kappa, \delta, \gamma - 2\beta_s)$, the equations for the *CP* coefficients in terms of these physical variables reported in Eq. (12), $P(\Lambda)$, need to be inverted. This is accomplished by minimising the likelihood function [83]

$$-2\mathcal{L}(\Lambda) = -2\,\exp\left(-\frac{1}{2}(P(\Lambda) - P_{\mathrm{obs}})^T\, V^{-1}\,(P(\Lambda) - P_{\mathrm{obs}})\right). \tag{16}$$

Here, V denotes the experimental (statistical and systematic) covariance matrix of the measured observables, see Appendix C. Figure 8 displays the confidence levels (CL) for the physical parameters Λ obtained from the model-independent method, where the physical boundary of the coherence factor is enforced. The $1 - \mathrm{CL} = 68.3\%$ (1σ) confidence intervals are given in Table 6 together with the results of the full time-dependent amplitude analysis. Considering the difference in statistical sensitivity of the two methods and that the model-dependent uncertainty only affects the full time-dependent amplitude fit, a good agreement between the measurements is observed. As a cross-check, pseudoexperiments are performed to study the distribution of the test statistic $Q^2 = \sum_i (\Lambda_i^{\mathrm{MI}} - \Lambda_i^{\mathrm{MD}})^2/(\sigma_{\mathrm{stat}}(\Lambda_i^{\mathrm{MI}})^2 - \sigma_{\mathrm{stat}}(\Lambda_i^{\mathrm{MD}})^2)$, where Λ_i^{MI} $(\Lambda_i^{\mathrm{MD}})$ and $\sigma_{\mathrm{stat}}(\Lambda_i^{\mathrm{MI}})$ $(\sigma_{\mathrm{stat}}(\Lambda_i^{\mathrm{MD}}))$ denote the measured value of the physical observable Λ_i and its statistical

uncertainty obtained with the model-independent (model-dependent) method. It is found that $p = 33\%$ of the pseudoexperiments have a larger Q^2 value than observed on data, considering only the statistical uncertainty. The p-value increases to $p = 49\%$ when the uncertainty due to the amplitude modelling is included.

The measured ratio of the $b \to u$ and $b \to c$ decay amplitudes is qualitatively consistent with the naive expectation based on the involved CKM elements ($r \approx 0.4$). Note that the parameters r, κ and δ are determined in a limited phase-space region (*cf.* Sec. 3.1) and might differ when the full phase space is considered.

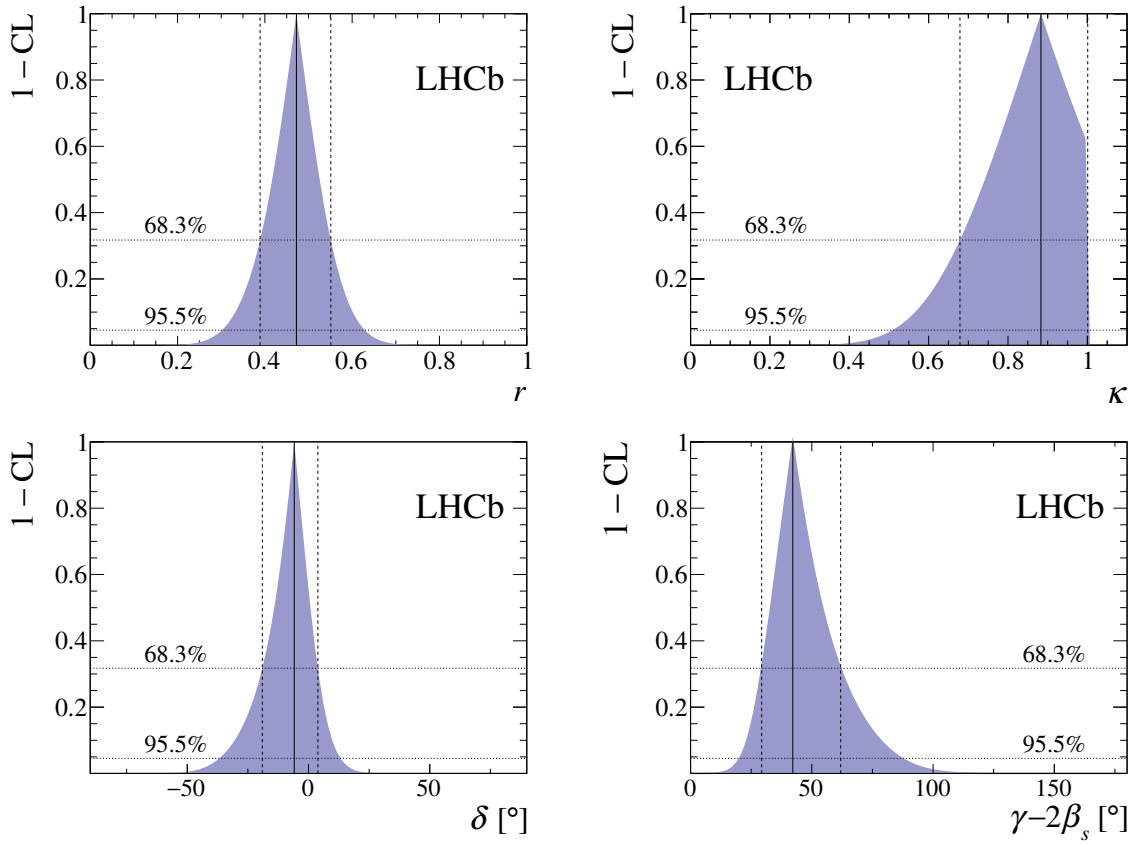

Figure 8: The 1−CL contours for the physical observables r, κ, δ and $\gamma - 2\beta_s$ obtained with the model-independent fit.

Table 6: Parameters determined from the model-independent and model-dependent fits to the $B_s^0 \to D_s^{\mp} K^{\pm}\pi^{\pm}\pi^{\mp}$ signal candidates. The uncertainties are statistical, systematic and (if applicable) due to alternative amplitude models considered. The angles are given modulo 180°.

Parameter	Model-independent	Model-dependent
r	$0.47^{+0.08}_{-0.08}{}^{+0.02}_{-0.03}$	$0.56 \pm 0.05 \pm 0.04 \pm 0.07$
κ	$0.88^{+0.12}_{-0.19}{}^{+0.04}_{-0.07}$	$0.72 \pm 0.04 \pm 0.06 \pm 0.04$
δ [°]	$-6\ ^{+10}_{-12}\ ^{+2}_{-4}$	$-14 \pm 10 \pm 4 \pm 5$
$\gamma - 2\beta_s$ [°]	$42\ ^{+19}_{-13}\ ^{+6}_{-2}$	$42 \pm 10 \pm 4 \pm 5$

8 Conclusion

Mixing-induced *CP* violation in $B_s^0 \to D_s^{\mp} K^{\pm}\pi^{\pm}\pi^{\mp}$ decays is studied for the first time using $9\,\text{fb}^{-1}$ of proton-proton collision data recorded by the LHCb detector. A time-dependent amplitude analysis is performed, disentangling the various intermediate-state components contributing via $b \to c$ or $b \to u$ quark-level transitions. The *CP*-violating weak phase $\gamma - 2\beta_s$ is measured and used to determine the CKM angle γ by taking the mixing phase, $-2\beta_s = \phi_s = (-2.35 \pm 1.43)^\circ$ [10], as an external input. This results in a measured value of $\gamma = (44 \pm 12)^\circ$ modulo 180°. A model-independent fit to the phase-space integrated decay-time spectrum yields a compatible, but statistically less precise, value of $\gamma = (44^{+20}_{-13})^\circ$ modulo 180°. These results correspond to 4.4σ and 4.6σ evidence for mixing-induced *CP* violation and agree with the world-average value of the CKM angle γ [2,3] within 2.2σ and 1.4σ for the model-dependent and model-independent methods, respectively. The $B_s^0 - \overline{B}_s^0$ oscillation frequency is measured from flavour-specific $B_s^0 \to D_s^-\pi^+\pi^+\pi^-$ decays to be $\Delta m_s = (17.757 \pm 0.007 \pm 0.008)\,\text{ps}^{-1}$. This is the most precise measurement of this quantity and consistent with the world-average value [2] and theoretical predictions [84]. Both the measurement of the CKM angle γ and of the $B_s^0 - \overline{B}_s^0$ mixing frequency are vital inputs for global fits of the CKM matrix.

Acknowledgements

We express our gratitude to our colleagues in the CERN accelerator departments for the excellent performance of the LHC. We thank the technical and administrative staff at the LHCb institutes. We acknowledge support from CERN and from the national agencies: CAPES, CNPq, FAPERJ and FINEP (Brazil); MOST and NSFC (China); CNRS/IN2P3 (France); BMBF, DFG and MPG (Germany); INFN (Italy); NWO (Netherlands); MNiSW and NCN (Poland); MEN/IFA (Romania); MSHE (Russia); MICINN (Spain); SNSF and SER (Switzerland); NASU (Ukraine); STFC (United Kingdom); DOE NP and NSF (USA). We acknowledge the computing resources that are provided by CERN, IN2P3 (France), KIT and DESY (Germany), INFN (Italy), SURF (Netherlands), PIC (Spain), GridPP (United Kingdom), RRCKI and Yandex LLC (Russia), CSCS (Switzerland), IFIN-HH (Romania), CBPF (Brazil), PL-GRID (Poland) and OSC (USA). We are indebted to the communities behind the multiple open-source software packages on which we depend. Individual groups or members have received support from AvH Foundation (Germany); EPLANET, Marie Skłodowska-Curie Actions and ERC (European Union); A*MIDEX, ANR, Labex P2IO and OCEVU, and Région Auvergne-Rhône-Alpes (France); Key Research Program of Frontier Sciences of CAS, CAS PIFI, Thousand Talents Program, and Sci. & Tech. Program of Guangzhou (China); RFBR, RSF and Yandex LLC (Russia); GVA, XuntaGal and GENCAT (Spain); the Royal Society and the Leverhulme Trust (United Kingdom).

Appendices

A Lineshapes

Lineshape parameters for resonances contributing to $B_s^0 \to D_s^\mp K^\pm \pi^\pm \pi^\mp$ decays are fixed to the values given in Table A.1. The running-width distributions of the three-body resonances are shown in Figure 9.

Table A.1: Parameters of the resonances included in the $B_s^0 \to D_s^\mp K^\pm \pi^\pm \pi^\mp$ baseline model.

Resonance	m_0 [MeV]	Γ_0 [MeV]	J^P	Source
$\rho(770)^0$	775.26 ± 0.25	149.1 ± 0.8	1^-	[2]
$K^*(892)^0$	895.55 ± 0.20	47.3 ± 0.5	1^-	[2]
$K_1(1270)^+$	1289.81 ± 1.75	116.11 ± 3.4	1^+	[85]
$K(1460)^+$	1482.4 ± 15.6	335.6 ± 10.6	0^-	[85]
$K_0^*(1430)^0$	1425 ± 50	270 ± 80	0^+	[2]

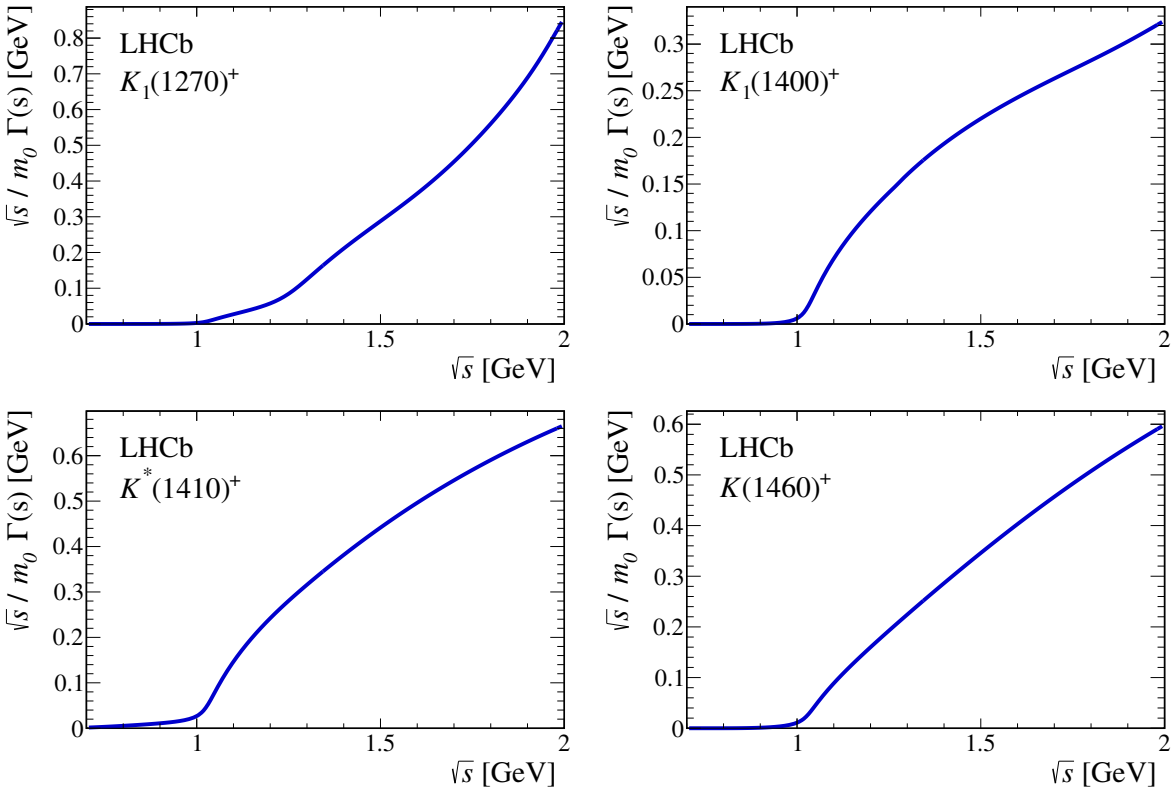

Figure 9: Running width distributions of the three-body resonances included in the baseline model for $B_s^0 \to D_s^\mp K^\pm \pi^\pm \pi^\mp$ decays: (top left) $K_1(1270)^+$, (top right) $K_1(1400)^+$, (bottom left) $K^*(1410)^+$ and (bottom right) $K(1460)^+$.

B Amplitude model

The full list of intermediate-state amplitudes considered for the model building procedure is given in Table B.1. In addition to those, the presence of unknown states decaying into $D_s^-\pi^+\pi^-$, $D_s^-K^+\pi^-$, $D_s^-\pi^+$ or $D_s^-K^+$ is investigated. These states are typically fitted with huge decay widths (effectively indistinguishable from a non-resonant state) and small decay fractions. Therefore, such states (if existent in the relevant mass range) are not resolvable with the current data sample.

Table B.1: Intermediate-state components considered for the $B_s^0 \to D_s^\mp K^\pm\pi^\pm\pi^\mp$ LASSO model building procedure. The letters in square brackets and subscripts refer to the relative orbital angular momentum of the decay products in spectroscopic notation. If no angular momentum is specified, the lowest angular momentum state compatible with angular momentum conservation and, where appropriate, parity conservation, is used.

(a) Cascade decays

$B_s^0 \to D_s^\mp\,[K_1(1270)^\pm[S,D] \to \pi^\pm\,K^*(892)^0]$
$B_s^0 \to D_s^\mp\,[K_1(1270)^\pm \to \pi^\pm\,K_0^*(1430)^0]$
$B_s^0 \to D_s^\mp\,[K_1(1270)^\pm \to K^\pm\,f_0(500)^0]$
$B_s^0 \to D_s^\mp\,[K_1(1270)^\pm \to K^\pm\,f_0(980)^0]$
$B_s^0 \to D_s^\mp\,[K_1(1270)^\pm[S,D] \to K^\pm\,\rho(770)^0]$
$B_s^0 \to D_s^\mp\,[K_1(1270)^\pm[S,D] \to K^\pm\,\rho(1450)^0]$
$B_s^0 \to D_s^\mp\,[K_1(1400)^\pm[S,D] \to \pi^\pm\,K^*(892)^0]$
$B_s^0 \to D_s^\mp\,[K_1(1400)^\pm[S,D] \to K^\pm\,\rho(770)^0]$
$B_s^0 \to D_s^\mp\,[K(1460)^\pm \to K^\pm\,f_0(500)^0]$
$B_s^0 \to D_s^\mp\,[K(1460)^\pm \to K^\pm\,\rho(770)^0]$
$B_s^0 \to D_s^\mp\,[K(1460)^\pm \to \pi^\pm\,K^*(892)^0]$
$B_s^0 \to D_s^\mp\,[K(1460)^\pm \to \pi^\pm\,K^*(1430)^0]$
$B_s^0 \to D_s^\mp\,[K^*(1410)^\pm \to \pi^\pm\,K^*(892)^0]$
$B_s^0 \to D_s^\mp\,[K^*(1410)^\pm \to K^\pm\,\rho(770)^0]$
$B_s^0 \to D_s^\mp\,[K_2^*(1430)^\pm \to \pi^\pm\,K^*(892)^0]$
$B_s^0 \to D_s^\mp\,[K_2^*(1430)^\pm \to K^\pm\,\rho(770)^0]$
$B_s^0 \to D_s^\mp\,[K_1(1650)^\pm \to \pi^\pm\,K^*(892)^0]$
$B_s^0 \to D_s^\mp\,[K_1(1650)^\pm \to K^\pm\,\rho(770)^0]$
$B_s^0 \to D_s^\mp\,[K^*(1680)^\pm \to \pi^\pm\,K^*(892)^0]$
$B_s^0 \to D_s^\mp\,[K^*(1680)^\pm \to K^\pm\,\rho(770)^0]$
$B_s^0 \to D_s^\mp\,[K_2(1770)^\pm \to \pi^\pm\,K^*(892)^0]$
$B_s^0 \to D_s^\mp\,[K_2(1770)^\pm \to K^\pm\,\rho(770)^0]$
$B_s^0 \to D_s^\mp\,[K_2(1770)^\pm \to \pi^\pm\,K_2^*(1430)^0]$
$B_s^0 \to D_s^\mp\,[K_2(1770)^\pm \to K^\pm\,f_2(1270)^0]$
$B_s^0 \to D_s^\mp\,[K_2^*(1980)^\pm \to \pi^\pm\,K^*(892)^0]$
$B_s^0 \to D_s^\mp\,[K_2^*(1980)^\pm \to K^\pm\,\rho(770)^0]$
$B_s^0 \to D_s^\mp\,[K_2^*(1980)^\pm \to \pi^\pm\,K_2^*(1430)^0]$
$B_s^0 \to D_s^\mp\,[K_2^*(1980)^\pm \to K^\pm\,f_2(1270)]$
$B_s^0 \to K^\pm[D_{s1}(2536)^\mp \to D_s^\mp\;\rho(770)^0]$
$B_s^0 \to K^\pm[D_{s1}(2536)^\mp \to D_s^\mp\;f_0(500)^0]$

(b) Quasi-two-body decays

$B_s^0 \to f_0(500)^0(D_s^\mp K^\pm)_S$
$B_s^0 \to f_0(500)^0(D_s^\mp K^\pm)_P$
$B_s^0 \to f_0(980)^0(D_s^\mp K^\pm)_S$
$B_s^0 \to f_0(980)^0(D_s^\mp K^\pm)_P$
$B_s^0 \to \rho(770)^0(D_s^\mp K^\pm)_S$
$B_s^0[S,P,D] \to \rho(770)^0\,(D_s^\mp K^\pm)_P$
$B_s^0 \to f_2(1270)^0(D_s^\mp K^\pm)_S$
$B_s^0 \to K^*(892)^0\,(D_s^\mp\pi^\pm)_S$
$B_s^0[S,P,D] \to K^*(892)^0\,(D_s^\mp\pi^\pm)_P$
$B_s^0 \to K_0^*(1430)^0\,(D_s^\mp\pi^\pm)_S$
$B_s^0 \to K_2^*(1430)^0\,(D_s^\mp\pi^\pm)_S$
$B_s^0 \to (D_s^\mp K^\pm)_S\,(\pi^\pm\pi^\mp)_S$

Tables B.2 and B.3 list the moduli and phases of the complex amplitude coefficients obtained by fitting the baseline model to the background-subtracted $B_s^0 \to D_s^\mp K^\pm \pi^\pm \pi^\mp$ signal candidates. The systematic uncertainties are summarised in Table B.4. The fit results are used to derive the amplitude ratio, r_i, and strong-phase difference, δ_i, for a given decay channel, defined as

$$r_i = r \left| \frac{a_i^u}{a_i^c} \right| \sqrt{\frac{\int |A^c(\mathbf{x})|^2 \, \mathrm{d}\Phi_4(\mathbf{x})}{\int |A^u(\mathbf{x})|^2 \, \mathrm{d}\Phi_4(\mathbf{x})}},$$

$$\delta_i = \delta - \arg(a_i^c) + \arg(a_i^u) - \arg\left(\int A^c(\mathbf{x})^* \, A^u(\mathbf{x}) \, \mathrm{d}\Phi_4(\mathbf{x}) \right).$$

The values are given in Table B.5. Tables B.6 ($b \to c$ amplitudes) and B.7 ($b \to u$ amplitudes) list the interference fractions ordered by magnitude, for the baseline model. Figures 10 and 11 show additional fit projections of the baseline model. Here, the acoplanarity angle, $\phi_{K^+\pi^-, D_s^-\pi^+}$, is defined as the angle between the two decay planes formed by the $K^+\pi^-$ system and the $D_s^-\pi^+$ system in the B_s^0 rest frame; boosting into the rest frames of the two-body systems defining these decay planes, the two helicity variables $\cos\theta_{K^+\pi^-}$ and $\cos\theta_{D_s^-\pi^+}$ are defined as the cosine of the angle of the K^+ or D_s^- momentum with the B_s^0 flight direction.

The decay fractions for several alternative models are summarised in Tables B.8 and B.9.

Table B.2: Moduli and phases of the amplitude coefficients for decays via $b \to c$ and $b \to u$ quark-level transitions. The uncertainties are statistical and systematic.

Decay channel	$A^c(\mathbf{x})$		$A^u(\mathbf{x})$	
	$\lvert a_i^c \rvert$	$\arg(a_i^c)[^\circ]$	$\lvert a_i^u \rvert$	$\arg(a_i^u)[^\circ]$
$B_s^0 \to D_s^\mp K_1(1270)^\pm$	$0.50 \pm 0.05 \pm 0.05$	$24 \pm 4 \pm 6$	$0.51 \pm 0.27 \pm 0.25$	$-129 \pm 18 \pm 26$
$B_s^0 \to D_s^\mp K_1(1400)^\pm$	1.0	0.0	1.0	0.0
$B_s^0 \to D_s^\mp K^*(1410)^\pm$	$0.45 \pm 0.05 \pm 0.05$	$53 \pm 6 \pm 6$	$0.81 \pm 0.20 \pm 0.15$	$2 \pm 13 \pm 11$
$B_s^0 \to D_s^\mp K(1460)^\pm$			$0.78 \pm 0.20 \pm 0.16$	$-92 \pm 10 \pm 15$
$B_s^0 \to (D_s^\mp \pi^\pm)_P K^*(892)^0$	$0.40 \pm 0.04 \pm 0.04$	$-33 \pm 5 \pm 4$	$1.21 \pm 0.26 \pm 0.22$	$-7 \pm 8 \pm 17$
$B_s^0 \to (D_s^\mp K^\pm)_P \rho(770)^0$	$0.12 \pm 0.03 \pm 0.03$	$109 \pm 9 \pm 14$		

Table B.3: Moduli and phases of the amplitude coefficients for cascade decays. The amplitude coefficients are defined relative to the respective three-body production amplitude coefficients in Table B.2 and are shared among $b \to c$ and $b \to u$ transitions. The uncertainties are statistical and systematic.

Decay channel	$\lvert a_i \rvert$	$\arg(a_i)[^\circ]$
$K_1(1270)^\pm \to K^\pm \rho(770)^0$	1.0	0.0
$K_1(1270)^\pm \to K^*(892)^0 \pi^\pm$	$0.90 \pm 0.09 \pm 0.10$	$46 \pm 7 \pm 4$
$K_1(1270)^\pm \to K_0^*(1430)^0 \pi^\pm$	$0.46 \pm 0.05 \pm 0.03$	$120 \pm 5 \pm 6$
$K^*(1410)^\pm \to K^*(892)^0 \pi^\pm$	1.0	0.0
$K^*(1410)^\pm \to K^\pm \rho(770)^0$	$0.66 \pm 0.05 \pm 0.05$	$-165 \pm 6 \pm 5$

Table B.4: Systematic uncertainties on the fit parameters of the full time-dependent amplitude fit to $B_s^0 \to D_s^\mp K^\pm \pi^\pm \pi^\mp$ data in units of the statistical standard deviations. The different contributions are: 1) fit bias, 2) background subtraction, 3) correlation of observables, 4) time acceptance, 5) resolution, 6) decay-time bias, 7) nuisance asymmetries, 8) Δm_s, 9) phase-space acceptance, 10) acceptance factorisation, 11) lineshape models, 12) masses and widths of resonances, 13) form factor.

Parameter	1	2	3	4	5	6	7	8	9	10	11	12	13	Total
$B_s^0 \to D_s^\mp K_1(1270)^\pm \lvert a_i^c \rvert$	0.09	0.32	0.17	0.01	0.36	0.05	0.00	0.02	0.60	0.11	0.31	0.07	0.48	0.99
$B_s^0 \to D_s^\mp K_1(1270)^\pm \arg(a_i^c)$	0.10	0.37	0.12	0.03	0.13	0.05	0.05	0.02	0.40	0.31	0.98	0.21	0.58	1.33
$B_s^0 \to D_s^\mp K_1(1270)^\pm \lvert a_i^u \rvert$	0.17	0.26	0.14	0.04	0.41	0.07	0.01	0.03	0.35	0.18	0.60	0.02	0.26	0.94
$B_s^0 \to D_s^\mp K_1(1270)^\pm \arg(a_i^u)$	0.12	0.77	0.21	0.08	0.39	0.05	0.11	0.04	0.66	0.55	0.52	0.07	0.54	1.46
$K_1(1270)^\pm \to K^*(892)^0 \pi^\pm \lvert a_i \rvert$	0.01	0.32	0.27	0.01	0.31	0.01	0.00	0.01	0.17	0.36	0.55	0.15	0.55	1.03
$K_1(1270)^\pm \to K^*(892)^0 \pi^\pm \arg(a_i)$	0.14	0.11	0.11	0.01	0.13	0.02	0.00	0.00	0.19	0.14	0.33	0.07	0.34	0.59
$K_1(1270)^\pm \to K_0^*(1430)^0 \pi^\pm \lvert a_i \rvert$	0.10	0.48	0.14	0.00	0.05	0.01	0.00	0.00	0.10	0.25	0.42	0.05	0.17	0.73
$K_1(1270)^\pm \to K_0^*(1430)^0 \pi^\pm \arg(a_i)$	0.24	0.33	0.53	0.00	0.14	0.01	0.00	0.00	0.27	0.46	0.16	0.08	0.85	1.22
$B_s^0 \to D_s^\mp K^*(1410)^\pm \lvert a_i^c \rvert$	0.27	0.35	0.14	0.02	0.29	0.04	0.00	0.01	0.87	0.32	0.09	0.10	0.20	1.10
$B_s^0 \to D_s^\mp K^*(1410)^\pm \arg(a_i^c)$	0.32	0.29	0.10	0.01	0.40	0.02	0.00	0.01	0.23	0.21	0.46	0.06	0.64	1.04
$B_s^0 \to D_s^\mp K^*(1410)^\pm \lvert a_i^u \rvert$	0.17	0.16	0.17	0.03	0.25	0.07	0.07	0.03	0.38	0.32	0.26	0.05	0.34	0.77
$B_s^0 \to D_s^\mp K^*(1410)^\pm \arg(a_i^u)$	0.21	0.42	0.41	0.05	0.13	0.01	0.01	0.01	0.07	0.26	0.21	0.05	0.47	0.87
$K^*(1410)^\pm \to K^\pm \rho(770)^0 \lvert a_i \rvert$	0.58	0.37	0.26	0.00	0.19	0.02	0.10	0.00	0.43	0.45	0.31	0.04	0.06	1.03
$K^*(1410)^\pm \to K^\pm \rho(770)^0 \arg(a_i)$	0.05	0.42	0.24	0.00	0.19	0.04	0.06	0.00	0.58	0.03	0.22	0.05	0.19	0.84
$B_s^0 \to D_s^\mp K(1460)^\pm \lvert a_i^u \rvert$	0.02	0.22	0.28	0.05	0.13	0.04	0.01	0.02	0.22	0.18	0.63	0.04	0.19	0.82
$B_s^0 \to D_s^\mp K(1460)^\pm \arg(a_i^u)$	0.14	0.51	0.10	0.06	0.30	0.01	0.19	0.02	0.39	0.48	0.11	0.10	1.15	1.46
$B_s^0 \to (D_s^\mp \pi^\pm)_P \ K^*(892)^0 \lvert a_i^c \rvert$	0.06	0.37	0.11	0.01	0.13	0.05	0.01	0.02	0.09	0.32	0.58	0.09	0.62	1.00
$B_s^0 \to (D_s^\mp \pi^\pm)_P \ K^*(892)^0 \arg(a_i^c)$	0.03	0.60	0.29	0.03	0.19	0.04	0.02	0.02	0.22	0.10	0.43	0.06	0.29	0.90
$B_s^0 \to (D_s^\mp \pi^\pm)_P \ K^*(892)^0 \lvert a_i^u \rvert$	0.08	0.26	0.15	0.05	0.20	0.02	0.01	0.02	0.18	0.26	0.62	0.04	0.33	0.86
$B_s^0 \to (D_s^\mp \pi^\pm)_P \ K^*(892)^0 \arg(a_i^u)$	0.20	0.75	0.66	0.05	0.54	0.06	0.15	0.04	0.36	0.68	0.31	0.13	1.37	1.98
$B_s^0 \to (D_s^\mp K^\pm)_P \ \rho(770)^0 \lvert a_i^c \rvert$	0.11	0.46	0.14	0.01	0.12	0.03	0.00	0.00	0.32	0.05	0.71	0.06	0.37	1.01
$B_s^0 \to (D_s^\mp K^\pm)_P \ \rho(770)^0 \arg(a_i^c)$	0.18	0.66	0.66	0.01	0.23	0.01	0.00	0.01	0.20	0.22	1.12	0.06	0.47	1.59

Table B.5: Amplitude ratio and strong-phase difference for a given decay channel. The uncertainties are statistical and systematic.

Decay channel	r_i	$\delta_i[^\circ]$
$B_s^0 \to D_s^\mp K_1(1270)^\pm$	$0.31 \pm 0.20 \pm 0.16$	$-109 \pm 22 \pm 28$
$B_s^0 \to D_s^\mp K_1(1400)^\pm$	$0.30 \pm 0.03 \pm 0.02$	$44 \pm 10 \pm 4$
$B_s^0 \to D_s^\mp K^*(1410)^\pm$	$0.54 \pm 0.18 \pm 0.15$	$-7 \pm 17 \pm 14$
$B_s^0 \to (D_s^\mp \pi^\pm)_P\ K^*(892)^0$	$0.92 \pm 0.24 \pm 0.20$	$69 \pm 15 \pm 18$

Table B.6: Interference fractions (ordered by magnitude) of the $b \to c$ intermediate-state amplitudes included in the baseline model. Only the statistical uncertainties are given.

Decay channel i	Decay channel j	$I_{ij}[\%]$
$B_s^0 \to D_s^\mp (K_1(1400)^\pm \to K^*(892)^0 \pi^\pm)$	$B_s^0 \to (D_s^\mp \pi^\pm)_P\ K^*(892)^0$	-15.4 ± 3.1
$B_s^0 \to D_s^\mp (K_1(1270)^\pm \to K^*(892)^0 \pi^\pm)$	$B_s^0 \to D_s^\mp (K_1(1400)^\pm \to K^*(892)^0 \pi^\pm)$	-12.2 ± 5.8
$B_s^0 \to D_s^\mp (K_1(1270)^\pm \to K^*(892)^0 \pi^\pm)$	$B_s^0 \to (D_s^\mp \pi^\pm)_P\ K^*(892)^0$	-10.2 ± 1.2
$B_s^0 \to D_s^\mp (K_1(1400)^\pm \to K^*(892)^0 \pi^\pm)$	$B_s^0 \to D_s^\mp (K_1(1270)^\pm \to K^\pm \rho(770)^0)$	5.8 ± 0.5
$B_s^0 \to D_s^\mp (K^*(1410)^\pm \to K^*(892)^0 \pi^\pm)$	$B_s^0 \to D_s^\mp (K^*(1410)^\pm \to K^\pm \rho(770)^0)$	4.1 ± 0.3
$B_s^0 \to (D_s^\mp K^\pm)_P\ \rho(770)^0$	$B_s^0 \to D_s^\mp (K_1(1270)^\pm \to K^\pm \rho(770)^0)$	3.1 ± 0.5
$B_s^0 \to D_s^\mp (K_1(1400)^\pm \to K^*(892)^0 \pi^\pm)$	$B_s^0 \to (D_s^\mp K^\pm)_P\ \rho(770)^0$	1.3 ± 0.3
$B_s^0 \to D_s^\mp (K_1(1270)^\pm \to K_0^*(1430) \pi^\pm)$	$B_s^0 \to D_s^\mp (K_1(1270)^\pm \to K^\pm \rho(770)^0)$	-1.3 ± 0.9
$B_s^0 \to (D_s^\mp K^\pm)_P\ \rho(770)^0$	$B_s^0 \to D_s^\mp (K_1(1270)^\pm \to K_0^*(1430) \pi^\pm)$	-0.5 ± 0.3
$B_s^0 \to (D_s^\mp \pi^\pm)_P\ K^*(892)^0$	$B_s^0 \to (D_s^\mp K^\pm)_P\ \rho(770)^0$	-0.2 ± 0.1
$B_s^0 \to D_s^\mp (K_1(1270)^\pm \to K^*(892)^0 \pi^\pm)$	$B_s^0 \to D_s^\mp (K_1(1270)^\pm \to K^\pm \rho(770)^0)$	-0.1 ± 0.5
$B_s^0 \to (D_s^\mp \pi^\pm)_P\ K^*(892)^0$	$B_s^0 \to D_s^\mp (K_1(1270)^\pm \to K^\pm \rho(770)^0)$	-0.1 ± 0.1
$B_s^0 \to D_s^\mp (K_1(1400)^\pm \to K^*(892)^0 \pi^\pm)$	$B_s^0 \to D_s^\mp (K_1(1270)^\pm \to K_0^*(1430) \pi^\pm)$	-0.1 ± 0.0
$B_s^0 \to D_s^\mp (K_1(1270)^\pm \to K^*(892)^0 \pi^\pm)$	$B_s^0 \to (D_s^\mp K^\pm)_P\ \rho(770)^0$	0.0 ± 0.1
$B_s^0 \to D_s^\mp (K_1(1400)^\pm \to K^*(892)^0 \pi^\pm)$	$B_s^0 \to D_s^\mp (K^*(1410)^\pm \to K^\pm \rho(770)^0)$	0.0 ± 0.0
$B_s^0 \to (D_s^\mp \pi^\pm)_P\ K^*(892)^0$	$B_s^0 \to D_s^\mp (K_1(1270)^\pm \to K_0^*(1430) \pi^\pm)$	0.0 ± 0.0
$B_s^0 \to D_s^\mp (K^*(1410)^\pm \to K^\pm \rho(770)^0)$	$B_s^0 \to D_s^\mp (K_1(1270)^\pm \to K^\pm \rho(770)^0)$	0.0 ± 0.0
$B_s^0 \to D_s^\mp (K_1(1400)^\pm \to K^*(892)^0 \pi^\pm)$	$B_s^0 \to D_s^\mp (K^*(1410)^\pm \to K^*(892)^0 \pi^\pm)$	0.0 ± 0.0
$B_s^0 \to (D_s^\mp \pi^\pm)_P\ K^*(892)^0$	$B_s^0 \to D_s^\mp (K^*(1410)^\pm \to K^\pm \rho(770)^0)$	0.0 ± 0.0
$B_s^0 \to D_s^\mp (K_1(1270)^\pm \to K^*(892)^0 \pi^\pm)$	$B_s^0 \to D_s^\mp (K_1(1270)^\pm \to K_0^*(1430) \pi^\pm)$	0.0 ± 0.0
$B_s^0 \to D_s^\mp (K^*(1410)^\pm \to K^*(892)^0 \pi^\pm)$	$B_s^0 \to D_s^\mp (K_1(1270)^\pm \to K_0^*(1430) \pi^\pm)$	0.0 ± 0.0
$B_s^0 \to D_s^\mp (K_1(1270)^\pm \to K^*(892)^0 \pi^\pm)$	$B_s^0 \to D_s^\mp (K^*(1410)^\pm \to K^\pm \rho(770)^0)$	0.0 ± 0.0
$B_s^0 \to D_s^\mp (K^*(1410)^\pm \to K^*(892)^0 \pi^\pm)$	$B_s^0 \to D_s^\mp (K_1(1270)^\pm \to K^\pm \rho(770)^0)$	0.0 ± 0.0
$B_s^0 \to D_s^\mp (K^*(1410)^\pm \to K^*(892)^0 \pi^\pm)$	$B_s^0 \to (D_s^\mp \pi^\pm)_P\ K^*(892)^0$	0.0 ± 0.0
$B_s^0 \to D_s^\mp (K^*(1410)^\pm \to K^\pm \rho(770)^0)$	$B_s^0 \to D_s^\mp (K_1(1270)^\pm \to K_0^*(1430) \pi^\pm)$	0.0 ± 0.0
$B_s^0 \to D_s^\mp (K^*(1410)^\pm \to K^*(892)^0 \pi^\pm)$	$B_s^0 \to (D_s^\mp K^\pm)_P\ \rho(770)^0$	0.0 ± 0.0
$B_s^0 \to D_s^\mp (K_1(1270)^\pm \to K^*(892)^0 \pi^\pm)$	$B_s^0 \to D_s^\mp (K^*(1410)^\pm \to K^*(892)^0 \pi^\pm)$	0.0 ± 0.0
$B_s^0 \to D_s^\mp (K^*(1410)^\pm \to K^\pm \rho(770)^0)$	$B_s^0 \to (D_s^\mp K^\pm)_P\ \rho(770)^0$	0.0 ± 0.0

Table B.7: Interference fractions (ordered by magnitude) of the $b \to u$ intermediate-state amplitudes included in the baseline model. Only the statistical uncertainties are given.

Decay channel i	Decay channel j	I_{ij} [%]
$B_s^0 \to D_s^\mp\,(K_1(1270)^\pm \to K^*(892)^0\,\pi^\pm)$	$B_s^0 \to (D_s^\mp\,\pi^\pm)_P\ K^*(892)^0$	9.5 ± 2.6
$B_s^0 \to D_s^\mp\,(K_1(1270)^\pm \to K^*(892)^0\,\pi^\pm)$	$B_s^0 \to D_s^\mp\,(K_1(1400)^\pm \to K^*(892)^0\,\pi^\pm)$	9.2 ± 3.2
$B_s^0 \to D_s^\mp\,(K(1460)^\pm \to K^*(892)^0\,\pi^\pm)$	$B_s^0 \to (D_s^\mp\,\pi^\pm)_P\ K^*(892)^0$	-5.5 ± 0.9
$B_s^0 \to D_s^\mp\,(K^*(1410)^\pm \to K^*(892)^0\,\pi^\pm)$	$B_s^0 \to D_s^\mp\,(K^*(1410)^\pm \to K^\pm\,\rho(770)^0)$	4.1 ± 0.8
$B_s^0 \to D_s^\mp\,(K_1(1400)^\pm \to K^*(892)^0\,\pi^\pm)$	$B_s^0 \to (D_s^\mp\,\pi^\pm)_P\ K^*(892)^0$	-3.7 ± 5.9
$B_s^0 \to D_s^\mp\,(K_1(1400)^\pm \to K^*(892)^0\,\pi^\pm)$	$B_s^0 \to D_s^\mp\,(K_1(1270)^\pm \to K^\pm\,\rho(770)^0)$	-1.2 ± 0.6
$B_s^0 \to D_s^\mp\,(K_1(1270)^\pm \to K_0^*(1430)\,\pi^\pm)$	$B_s^0 \to D_s^\mp\,(K_1(1270)^\pm \to K^\pm\,\rho(770)^0)$	-0.4 ± 0.3
$B_s^0 \to (D_s^\mp\,\pi^\pm)_P\ K^*(892)^0$	$B_s^0 \to D_s^\mp\,(K_1(1270)^\pm \to K^\pm\,\rho(770)^0)$	0.1 ± 0.3
$B_s^0 \to D_s^\mp\,(K^*(1410)^\pm \to K^*(892)^0\,\pi^\pm)$	$B_s^0 \to (D_s^\mp\,\pi^\pm)_P\ K^*(892)^0$	-0.1 ± 0.0
$B_s^0 \to (D_s^\mp\,\pi^\pm)_P\ K^*(892)^0$	$B_s^0 \to D_s^\mp\,(K^*(1410)^\pm \to K^\pm\,\rho(770)^0)$	0.0 ± 0.0
$B_s^0 \to D_s^\mp\,(K_1(1270)^\pm \to K^*(892)^0\,\pi^\pm)$	$B_s^0 \to D_s^\mp\,(K_1(1270)^\pm \to K^\pm\,\rho(770)^0)$	0.0 ± 0.2
$B_s^0 \to (D_s^\mp\,\pi^\pm)_P\ K^*(892)^0$	$B_s^0 \to D_s^\mp\,(K_1(1270)^\pm \to K_0^*(1430)\,\pi^\pm)$	0.0 ± 0.0
$B_s^0 \to D_s^\mp\,(K(1460)^\pm \to K^*(892)^0\,\pi^\pm)$	$B_s^0 \to D_s^\mp\,(K_1(1270)^\pm \to K^\pm\,\rho(770)^0)$	0.0 ± 0.0
$B_s^0 \to D_s^\mp\,(K^*(1410)^\pm \to K^*(892)^0\,\pi^\pm)$	$B_s^0 \to D_s^\mp\,(K_1(1270)^\pm \to K^\pm\,\rho(770)^0)$	0.0 ± 0.0
$B_s^0 \to D_s^\mp\,(K_1(1400)^\pm \to K^*(892)^0\,\pi^\pm)$	$B_s^0 \to D_s^\mp\,(K(1460)^\pm \to K^*(892)^0\,\pi^\pm)$	0.0 ± 0.0
$B_s^0 \to D_s^\mp\,(K_1(1270)^\pm \to K^*(892)^0\,\pi^\pm)$	$B_s^0 \to D_s^\mp\,(K(1460)^\pm \to K^*(892)^0\,\pi^\pm)$	0.0 ± 0.0
$B_s^0 \to D_s^\mp\,(K_1(1400)^\pm \to K^*(892)^0\,\pi^\pm)$	$B_s^0 \to D_s^\mp\,(K^*(1410)^\pm \to K^*(892)^0\,\pi^\pm)$	0.0 ± 0.0
$B_s^0 \to D_s^\mp\,(K(1460)^\pm \to K^*(892)^0\,\pi^\pm)$	$B_s^0 \to D_s^\mp\,(K^*(1410)^\pm \to K^\pm\,\rho(770)^0)$	0.0 ± 0.0
$B_s^0 \to D_s^\mp\,(K_1(1400)^\pm \to K^*(892)^0\,\pi^\pm)$	$B_s^0 \to D_s^\mp\,(K^*(1410)^\pm \to K^\pm\,\rho(770)^0)$	0.0 ± 0.0
$B_s^0 \to D_s^\mp\,(K^*(1410)^\pm \to K^\pm\,\rho(770)^0)$	$B_s^0 \to D_s^\mp\,(K_1(1270)^\pm \to K^\pm\,\rho(770)^0)$	0.0 ± 0.0
$B_s^0 \to D_s^\mp\,(K_1(1400)^\pm \to K^*(892)^0\,\pi^\pm)$	$B_s^0 \to D_s^\mp\,(K_1(1270)^\pm \to K_0^*(1430)\,\pi^\pm)$	0.0 ± 0.0
$B_s^0 \to D_s^\mp\,(K_1(1270)^\pm \to K^*(892)^0\,\pi^\pm)$	$B_s^0 \to D_s^\mp\,(K^*(1410)^\pm \to K^\pm\,\rho(770)^0)$	0.0 ± 0.0
$B_s^0 \to D_s^\mp\,(K^*(1410)^\pm \to K^*(892)^0\,\pi^\pm)$	$B_s^0 \to D_s^\mp\,(K_1(1270)^\pm \to K_0^*(1430)\,\pi^\pm)$	0.0 ± 0.0
$B_s^0 \to D_s^\mp\,(K(1460)^\pm \to K^*(892)^0\,\pi^\pm)$	$B_s^0 \to D_s^\mp\,(K^*(1410)^\pm \to K^*(892)^0\,\pi^\pm)$	0.0 ± 0.0
$B_s^0 \to D_s^\mp\,(K_1(1270)^\pm \to K^*(892)^0\,\pi^\pm)$	$B_s^0 \to D_s^\mp\,(K_1(1270)^\pm \to K_0^*(1430)\,\pi^\pm)$	0.0 ± 0.0
$B_s^0 \to D_s^\mp\,(K(1460)^\pm \to K^*(892)^0\,\pi^\pm)$	$B_s^0 \to D_s^\mp\,(K_1(1270)^\pm \to K_0^*(1430)\,\pi^\pm)$	0.0 ± 0.0
$B_s^0 \to D_s^\mp\,(K_1(1270)^\pm \to K^*(892)^0\,\pi^\pm)$	$B_s^0 \to D_s^\mp\,(K^*(1410)^\pm \to K^*(892)^0\,\pi^\pm)$	0.0 ± 0.0
$B_s^0 \to D_s^\mp\,(K^*(1410)^\pm \to K^\pm\,\rho(770)^0)$	$B_s^0 \to D_s^\mp\,(K_1(1270)^\pm \to K_0^*(1430)\,\pi^\pm)$	0.0 ± 0.0

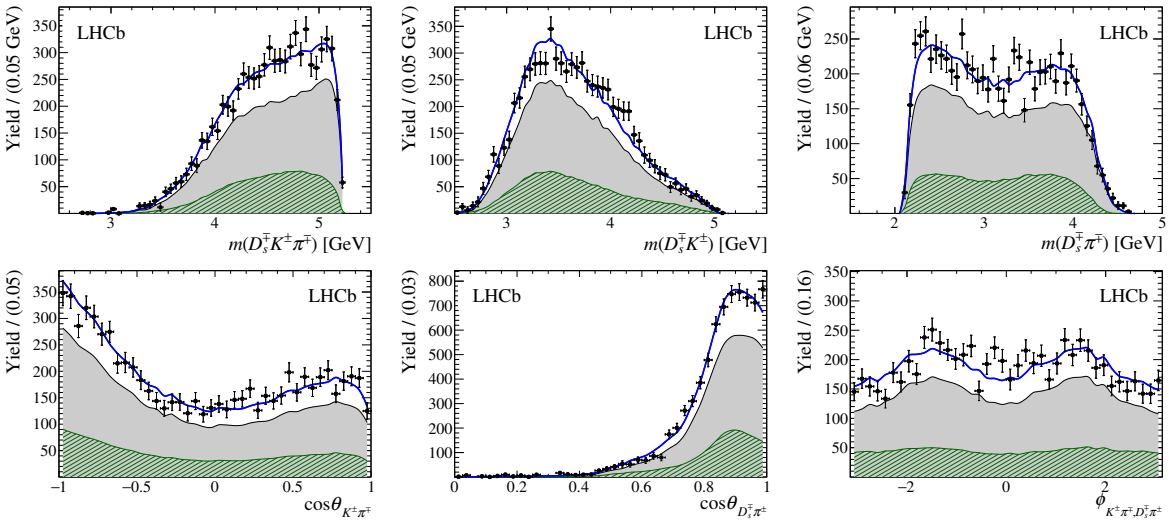

Figure 10: Invariant-mass and angular distributions of background-subtracted $B_s^0 \to D_s^\mp K^\pm \pi^\pm \pi^\mp$ candidates (data points) and fit projections (blue solid line). Contributions from $b \to c$ and $b \to u$ decay amplitudes are overlaid, colour coded as in Fig. 6.

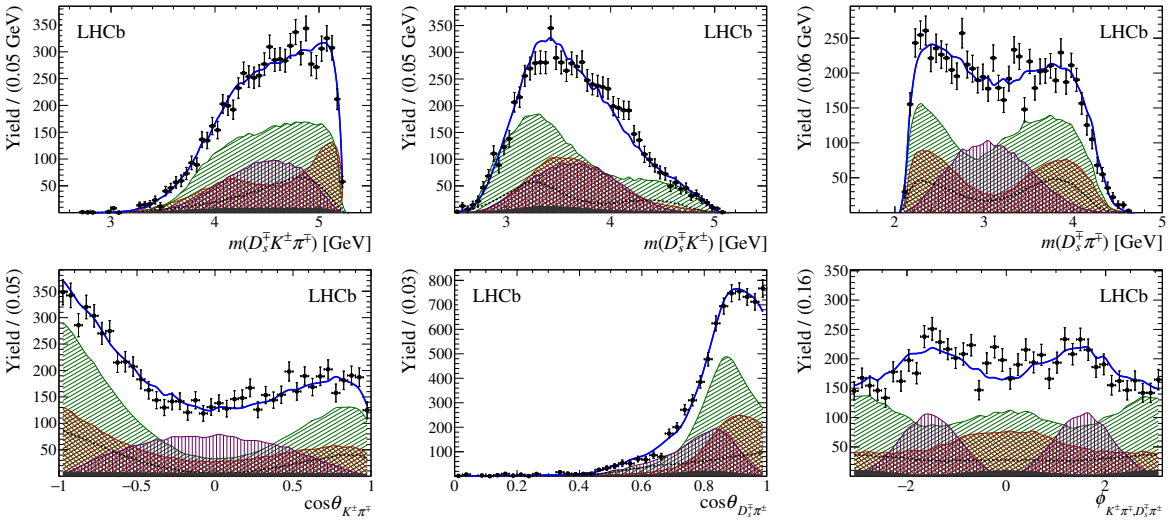

Figure 11: Invariant-mass and angular distributions of background-subtracted $B_s^0 \to D_s^\mp K^\pm \pi^\pm \pi^\mp$ candidates (data points) and fit projections (blue solid line). Incoherent contributions from intermediate-state components are overlaid, colour coded as in Fig. 7.

Table B.8: Decay fractions in percent for several alternative amplitude models (Alt. 1 - Alt. 6). Resonance parameters and the observables $r, \kappa, \delta, \gamma - 2\beta_s$ are also given.

		Alt.1	Alt.2	Alt.3	Alt.4	Alt.5	Alt.6
$b \to c$	$B_s^0 \to D_s^\mp\,(K_1(1270)^\pm \to K^*(892)^0\,\pi^\pm)$	12.2	12.0	13.9	11.5	14.7	12.8
	$B_s^0 \to D_s^\mp\,(K_1(1270)^\pm[D] \to K^*(892)^0\,\pi^\pm)$		0.4				
	$B_s^0 \to D_s^\mp\,(K_1(1270)^\pm \to K^\pm\,\rho(770)^0)$	16.2	14.6	21.7	15.6	18.6	16.5
	$B_s^0 \to D_s^\mp\,(K_1(1270)^\pm \to K^\pm\,\rho(1450)^0)$		0.3				
	$B_s^0 \to D_s^\mp\,(K_1(1270)^\pm \to K_0^*(1430)^0\,\pi^\pm)$	3.9	3.5	3.7	3.6	3.0	3.6
	$B_s^0 \to D_s^\mp\,(K_1(1400)^\pm \to K^*(892)^0\,\pi^\pm)$	43.1	61.1	59.8	57.7	69.5	60.6
	$B_s^0 \to D_s^\mp\,(K_1(1400)^\pm \to K^\pm\,\rho(770)^0)$			0.5			
	$B_s^0 \to D_s^\mp\,(K^*(1410)^\pm \to K^*(892)^0\,\pi^\pm)$	12.9	14.0	13.6	13.8	24.2	13.5
	$B_s^0 \to D_s^\mp\,(K^*(1410)^\pm \to K^\pm\,\rho(770)^0)$	4.9	5.8	4.9	5.3	3.6	5.2
	$B_s^0 \to D_s^\mp\,(K(1460)^\pm \to K^*(892)^0\,\pi^\pm)$	1.7			1.3		
	$B_s^0 \to D_s^\mp\,(K(1460)^\pm \to K^\pm\,\rho(770)^0)$				0.2		
	$B_s^0 \to D_s^\mp\,(K(1460)^\pm \to K^\pm\,f_0(500)^0)$				0.6		
	$B_s^0 \to D_s^\mp\,(K^*(1680)^\pm \to K^*(892)^0\,\pi^\pm)$					5.5	
	$B_s^0 \to D_s^\mp\,(K^*(1680)^\pm \to K^\pm\,\rho(770)^0)$					1.9	
	$B_s^0 \to D_s^\mp\,(K_2(1770) \to K^*(892)^0\,\pi^\pm)$						0.4
	$B_s^0 \to (D_s^\mp\,\pi^\pm)_P\;K^*(892)^0$	8.8	9.3	9.5	7.7	10.2	9.2
	$B_s^0 \to (D_s^\mp\,K^\pm)_P\;\rho(770)^0$	1.3	0.7	0.1	0.6	0.2	0.5
	Sum	105.1	121.7	127.6	118.0	151.5	122.1
$b \to u$	$B_s^0 \to D_s^\mp\,(K_1(1270)^\pm \to K^*(892)^0\,\pi^\pm)$	4.5	2.4	1.1	4.9	2.0	3.4
	$B_s^0 \to D_s^\mp\,(K_1(1270)^\pm[D] \to K^*(892)^0\,\pi^\pm)$		0.1				
	$B_s^0 \to D_s^\mp\,(K_1(1270)^\pm \to K^\pm\,\rho(770)^0)$	6.0	2.9	1.6	6.6	2.6	4.4
	$B_s^0 \to D_s^\mp\,(K_1(1270)^\pm \to K^\pm\,\rho(1450)^0)$		0.1				
	$B_s^0 \to D_s^\mp\,(K_1(1270)^\pm \to K_0^*(1430)^0\,\pi^\pm)$	1.4	0.7	0.3	1.5	0.4	1.0
	$B_s^0 \to D_s^\mp\,(K_1(1400)^\pm \to K^*(892)^0\,\pi^\pm)$	23.3	18.9	26.2	10.3	28.2	23.0
	$B_s^0 \to D_s^\mp\,(K_1(1400)^\pm \to K^\pm\,\rho(770)^0)$			0.2			
	$B_s^0 \to D_s^\mp\,(K^*(1410)^\pm \to K^*(892)^0\,\pi^\pm)$	14.8	13.7	12.7	7.2	2.4	11.5
	$B_s^0 \to D_s^\mp\,(K^*(1410)^\pm \to K^\pm\,\rho(770)^0)$	5.6	5.7	4.6	2.8	0.4	4.4
	$B_s^0 \to D_s^\mp\,(K(1460)^\pm \to K^*(892)^0\,\pi^\pm)$	12.9	10.8	12.6	8.1	12.1	11.9
	$B_s^0 \to D_s^\mp\,(K(1460)^\pm \to K^\pm\,\rho(770)^0)$				1.0		
	$B_s^0 \to D_s^\mp\,(K(1460)^\pm \to K^\pm\,f_0(500)^0)$				3.7		
	$B_s^0 \to D_s^\mp\,(K^*(1680)^\pm \to K^*(892)^0\,\pi^\pm)$					5.6	
	$B_s^0 \to D_s^\mp\,(K^*(1680)^\pm \to K^\pm\,\rho(770)^0)$					2.0	
	$B_s^0 \to D_s^\mp\,(K_2(1770) \to K^*(892)^0\,\pi^\pm)$						0.9
	$B_s^0 \to (D_s^\mp\,\pi^\pm)_P\;K^*(892)^0$	32.5	33.4	31.3	38.3	27.4	30.7
	Sum	103.9	88.7	90.7	84.4	83.0	91.4
	$m_{K_1(1400)}$ [MeV]	1401	1406	1404	1401	1397	1408
	$\Gamma_{K_1(1400)}$ [MeV]	189	193	192	196	199	193
	$m_{K^*(1410)}$ [MeV]	1434	1437	1436	1442	1419	1434
	$\Gamma_{K^*(1410)}$ [MeV]	391	400	386	382	453	395
	r	0.50	0.55	0.59	0.48	0.54	0.58
	κ	0.64	0.75	0.74	0.77	0.71	0.75
	$\delta\,[^\circ]$	-4	-15	-14	-24	-19	-18
	$\gamma - 2\beta_s\,[^\circ]$	40	44	42	50	52	51

Table B.9: Decay fractions in percent for several alternative amplitude models (Alt. 7 - Alt. 12). Resonance parameters and the observables $r, \kappa, \delta, \gamma - 2\beta_s$ are also given.

		Alt.7	Alt.8	Alt.9	Alt.10	Alt.11	Alt.12
$b \to c$	$B_s^0 \to D_s^\mp\,(K_1(1270)^\pm \to K^*(892)^0\,\pi^\pm)$	13.3	12.8	15.5	24.0	11.2	13.3
	$B_s^0 \to D_s^\mp\,(K_1(1270)^\pm \to K^\pm\,\rho(770)^0)$	17.5	17.5	19.1	14.9	17.7	19.9
	$B_s^0 \to D_s^\mp\,(K_1(1270)^\pm \to K_0^*(1430)^0\,\pi^\pm)$	3.3	4.0	4.3	2.8	3.2	3.7
	$B_s^0 \to D_s^\mp\,(K_1(1400)^\pm \to K^*(892)^0\,\pi^\pm)$	66.0	93.1	55.5	77.9	44.7	63.5
	$B_s^0 \to D_s^\mp\,(K^*(1410)^\pm \to K^*(892)^0\,\pi^\pm)$	12.5	16.5	13.3	13.7	15.1	12.7
	$B_s^0 \to D_s^\mp\,(K^*(1410)^\pm \to K^\pm\,\rho(770)^0)$	5.4	5.9	6.4	4.7	5.8	5.1
	$B_s^0 \to (D_s^\mp\,\pi^\pm)_S\ K^*(892)^0$				5.1		
	$B_s^0 \to (D_s^\mp\,\pi^\pm)_P\ K^*(892)^0$	11.4	19.8	8.5		5.5	10.8
	$B_s^0[P] \to (D_s^\mp\,\pi^\pm)_P\ K^*(892)^0$		1.7				
	$B_s^0[D] \to (D_s^\mp\,\pi^\pm)_P\ K^*(892)^0$		4.7				
	$B_s^0 \to (D_s^\mp\,K^\pm)_S\ f_0(500)^0$					1.8	
	$B_s^0 \to (D_s^\mp\,K^\pm)_S\ f_0(980)^0$					1.5	
	$B_s^0 \to (D_s^\mp\,K^\pm)_S\ f_2(1270)^0$					0.1	
	$B_s^0 \to (D_s^\mp\,K^\pm)_S\ \rho(770)^0$	0.3					
	$B_s^0 \to (D_s^\mp\,K^\pm)_P\ \rho(770)^0$		1.6	3.5	1.3	0.5	
	$B_s^0[P] \to (D_s^\mp\,K^\pm)_P\ \rho(770)^0$			0.2			
	$B_s^0[D] \to (D_s^\mp\,K^\pm)_P\ \rho(770)^0$			0.9			
	Sum	129.6	177.5	127.2	144.4	107.1	129.0
$b \to u$	$B_s^0 \to D_s^\mp\,(K_1(1270)^\pm \to K^*(892)^0\,\pi^\pm)$	3.3	5.2	1.1	10.6	2.5	2.5
	$B_s^0 \to D_s^\mp\,(K_1(1270)^\pm \to K^\pm\,\rho(770)^0)$	4.4	7.2	1.4	6.6	3.9	3.7
	$B_s^0 \to D_s^\mp\,(K_1(1270)^\pm \to K_0^*(1430)^0\,\pi^\pm)$	0.8	1.6	0.3	1.2	0.7	0.7
	$B_s^0 \to D_s^\mp\,(K_1(1400)^\pm \to K^*(892)^0\,\pi^\pm)$	19.8	35.8	27.8	7.7	17.1	22.4
	$B_s^0 \to D_s^\mp\,(K^*(1410)^\pm \to K^*(892)^0\,\pi^\pm)$	14.2	9.8	9.9	11.7	4.0	14.5
	$B_s^0 \to D_s^\mp\,(K^*(1410)^\pm \to K^\pm\,\rho(770)^0)$	6.1	3.5	4.8	4.0	1.5	5.8
	$B_s^0 \to D_s^\mp\,(K(1460)^\pm \to K^*(892)^0\,\pi^\pm)$	11.7	2.6	13.2	8.8	13.6	12.3
	$B_s^0 \to (D_s^\mp\,\pi^\pm)_S\ K^*(892)^0$				22.3		
	$B_s^0 \to (D_s^\mp\,\pi^\pm)_P\ K^*(892)^0$	25.8	68.5	33.6		43.1	29.3
	$B_s^0[P] \to (D_s^\mp\,\pi^\pm)_P\ K^*(892)^0$		5.8				
	$B_s^0[D] \to (D_s^\mp\,\pi^\pm)_P\ K^*(892)^0$		16.3				
	$B_s^0 \to (D_s^\mp\,K^\pm)_S\ f_0(500)^0$					0.7	
	$B_s^0 \to (D_s^\mp\,K^\pm)_S\ f_0(980)^0$					0.6	
	$B_s^0 \to (D_s^\mp\,K^\pm)_S\ f_2(1270)^0$					0.0	
	$B_s^0 \to (D_s^\mp\,K^\pm)_S\ \rho(770)^0$	0.4					
	$B_s^0 \to (D_s^\mp\,K^\pm)_P\ \rho(770)^0$			4.4			
	$B_s^0[P] \to (D_s^\mp\,K^\pm)_P\ \rho(770)^0$			0.3			
	$B_s^0[D] \to (D_s^\mp\,K^\pm)_P\ \rho(770)^0$			1.1			
	Sum	86.5	156.3	97.9	73.0	87.8	91.0
	$m_{K_1(1400)}$ [MeV]	1405	1398	1404	1365	1406	1406
	$\Gamma_{K_1(1400)}$ [MeV]	193	247	188	203	184	190
	$m_{K^*(1410)}$ [MeV]	1430	1443	1447	1440	1427	1434
	$\Gamma_{K^*(1410)}$ [MeV]	406	432	419	373	406	399
	r	0.57	0.75	0.58	0.45	0.54	0.57
	κ	0.73	0.81	0.73	0.70	0.75	0.73
	$\delta\,[^\circ]$	-16	-18	-12	-14	-19	-14
	$\gamma - 2\beta_s\,[^\circ]$	41	45	44	52	53	41

C Interpretation of the *CP* coefficients

The statistical and systematic correlation matrices of the *CP* coefficients obtained from the phase-space integrated fit are given in Table C.1 and Table C.2.

Figure 12 visualises the measured *CP* coefficients in the complex plane, where $\lambda_f \equiv (q/p)\,(\int A^u(\mathbf{x})\,\mathrm{d}\Phi_4 / \int A^c(\mathbf{x})\,\mathrm{d}\Phi_4)$. The points determined by $(-A_f^{\Delta\Gamma}, S_f)$ and $(-A_{\bar{f}}^{\Delta\Gamma}, S_{\bar{f}})$ are proportional to $r\,\kappa\,e^{\pm\delta-(\gamma-2\beta_s)}$, whilst an additional constraint on r arises from C_f.

Table C.1: Statistical correlation of the *CP* coefficients.

	C_f	$A_f^{\Delta\Gamma}$	$A_{\bar{f}}^{\Gamma\Delta}$	S_f	$S_{\bar{f}}$
C_f	1.000	0.135	0.168	0.040	0.042
$A_f^{\Delta\Gamma}$		1.000	0.504	−0.082	−0.052
$A_{\bar{f}}^{\Delta\Gamma}$			1.000	−0.036	−0.113
S_f				1.000	0.014
$S_{\bar{f}}$					1.000

Table C.2: Systematic correlation of the *CP* coefficients.

	C_f	$A_f^{\Delta\Gamma}$	$A_{\bar{f}}^{\Gamma\Delta}$	S_f	$S_{\bar{f}}$
C_f	1.000	0.039	0.042	−0.136	−0.006
$A_f^{\Delta\Gamma}$		1.000	0.208	−0.031	−0.023
$A_{\bar{f}}^{\Delta\Gamma}$			1.000	−0.021	−0.035
S_f				1.000	−0.278
$S_{\bar{f}}$					1.000

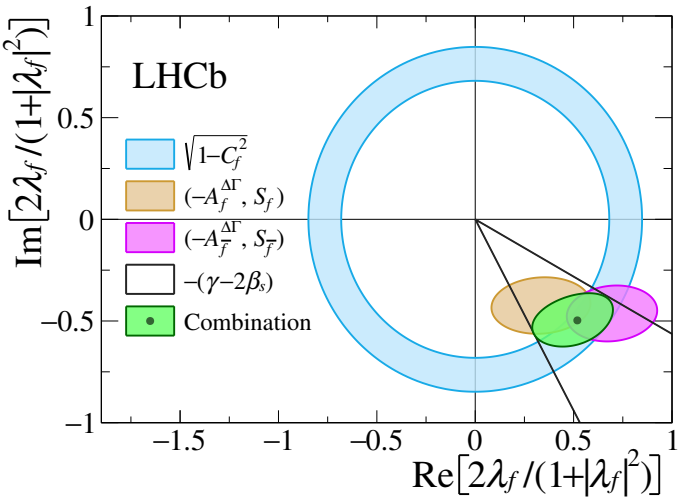

Figure 12: Visualisation of how the *CP* coefficients contribute towards the overall constraint on the weak phase, $\gamma - 2\beta_s$. The difference between the phase of $(-A_f^{\Delta\Gamma}, S_f)$ and $(-A_{\bar{f}}^{\Delta\Gamma}, S_{\bar{f}})$ is proportional to the strong phase δ, which is close to 0° and thus not indicated in the figure.

References

[1] N. Cabibbo, *Unitary symmetry and leptonic decays*, Phys. Rev. Lett. **10** (1963) 531; M. Kobayashi and T. Maskawa, *CP-violation in the renormalizable theory of weak interaction*, Prog. Theor. Phys. **49** (1973) 652.

[2] Particle Data Group, P. A. Zyla *et al.*, *Review of particle physics*, Prog. Theor. Exp. Phys. **2020** (2020) 083C01.

[3] Heavy Flavor Averaging Group, Y. Amhis *et al.*, *Averages of b-hadron, c-hadron, and τ-lepton properties as of 2018*, arXiv:1909.12524, updated results and plots available at https://hflav.web.cern.ch.

[4] LHCb collaboration, M. W. Kenzie and M. P. Whitehead, *Update of the LHCb combination of the CKM angle γ*, LHCb-CONF-2018-002, 2018.

[5] CKMfitter group, J. Charles *et al.*, *Current status of the standard model CKM fit and constraints on $\Delta F = 2$ new physics*, Phys. Rev. **D91** (2015) 073007, arXiv:1501.05013, updated results and plots available at http://ckmfitter.in2p3.fr/.

[6] UTfit collaboration, M. Bona *et al.*, *The unitarity triangle fit in the standard model and hadronic parameters from lattice QCD: A reappraisal after the measurements of Δm_s and $BR(B \to \tau\nu_\tau)$*, JHEP **10** (2006) 081, arXiv:hep-ph/0606167, updated results and plots available at http://www.utfit.org/.

[7] R. Fleischer, *New strategies to obtain insights into CP violation through $B_s \to D_s^\pm K^\mp, D_s^{*\pm} K^\mp$ and $B_d \to D^\pm \pi^\mp, D^{*\pm}\pi^\mp$ decays*, Nucl. Phys. **B671** (2003) 459, arXiv:hep-ph/0304027.

[8] K. De Bruyn *et al.*, *Exploring $B_s \to D_s^{(*)\pm} K^\mp$ decays in the presence of a sizable width difference $\Delta\Gamma_s$*, Nucl. Phys. **B868** (2013) 351, arXiv:1208.6463.

[9] LHCb collaboration, R. Aaij *et al.*, *Precision measurement of CP violation in $B_s^0 \to J/\psi K^+K^-$ decays*, Phys. Rev. Lett. **114** (2015) 041801, arXiv:1411.3104.

[10] LHCb collaboration, R. Aaij *et al.*, *Updated measurement of time-dependent CP-violating observables in $B_s^0 \to J/\psi K^+K^-$ decays*, Eur. Phys. J. **C79** (2019) 706, Erratum ibid. **C80** (2020) 601, arXiv:1906.08356.

[11] LHCb collaboration, R. Aaij *et al.*, *Measurement of the CP-violating phase ϕ_s in $\overline{B}_s^0 \to J/\psi\pi^+\pi^-$ decays*, Phys. Lett. **B736** (2014) 186, arXiv:1405.4140.

[12] LHCb collaboration, R. Aaij *et al.*, *Measurement of the CP violating phase and decay-width difference in $B_s^0 \to \psi(2S)\phi$ decays*, Phys. Lett. **B762** (2016) 253, arXiv:1608.04855.

[13] LHCb collaboration, R. Aaij *et al.*, *Measurement of the CP-violating phase ϕ_s in $\overline{B}_s^0 \to D_s^+ D_s^-$ decays*, Phys. Rev. Lett. **113** (2014) 211801, arXiv:1409.4619.

[14] LHCb collaboration, R. Aaij *et al.*, *Measurement of the CP-violating phase ϕ_s from $B_s^0 \to J/\psi\pi^+\pi^-$ decays in 13 TeV pp collisions*, Phys. Lett. **B797** (2019) 134789, arXiv:1903.05530.

[15] L. Wolfenstein, *Parametrization of the Kobayashi-Maskawa Matrix*, Phys. Rev. Lett. **51** (1983) 1945.

[16] LHCb collaboration, R. Aaij *et al.*, *Measurement of CP asymmetry in $B_s^0 \to D_s^\mp K^\pm$ decays*, JHEP **11** (2014) 060, arXiv:1407.6127.

[17] LHCb collaboration, R. Aaij *et al.*, *Measurement of CP asymmetry in $B_s^0 \to D_s^\mp K^\pm$ decays*, JHEP **03** (2018) 059, arXiv:1712.07428.

[18] LHCb collaboration, R. Aaij *et al.*, *First observation of the decays $\overline{B}{}^0_{(s)} \to D_s^+ K^-\pi^+\pi^-$ and $\overline{B}{}^0_s \to D_{s1}(2536)^+\pi^-$*, Phys. Rev. **D86** (2012) 112005, arXiv:1211.1541.

[19] S. Mandelstam, J. E. Paton, R. F. Peierls and A. Q. Sarker, *Isobar approximation of production processes*, Annals of Physics **18** (1962) 198 .

[20] D. J. Herndon, P. Söding, and R. J. Cashmore, *Generalized isobar model formalism*, Phys. Rev. D **11** (1975) 3165.

[21] J. J. Brehm, *Unitarity and the isobar model: two-body discontinuities*, Annals of Physics **108** (1977) 454 .

[22] F. von Hippel and C. Quigg, *Centrifugal-barrier effects in resonance partial decay widths, shapes, and production amplitudes*, Phys. Rev. D **5** (1972) 624.

[23] J. M. Blatt and V. F. Weisskopf, *Theoretical nuclear physics*, Springer, New York, 1952.

[24] J. D. Jackson, *Remarks on the phenomenological analysis of resonances*, Il Nuovo Cimento Series 10 **34** (1964) 1644.

[25] D. V. Bugg, *The mass of the σ pole*, Journal of Physics G Nuclear Physics **34** (2007) 151, arXiv:hep-ph/0608081.

[26] D. Aston *et al.*, *A study of $K^-\pi^+$ scattering in the reaction $K^-p \to K^-\pi^+n$ at $11GeV/c$*, Nucl. Phys. **B296** (1988) 493.

[27] BaBar collaboration, B. Aubert *et al.*, *Dalitz-plot analysis of the decays $B^\pm \to K^\pm\pi^\mp\pi^\pm$*, Phys. Rev. **D72** (2005) 072003, arXiv:hep-ex/0507004, [Erratum: Phys. Rev.D74,099903(2006)].

[28] G. J. Gounaris and J. J. Sakurai, *Finite-width corrections to the vector-meson-dominance prediction for $\rho \to e^+e^-$*, Phys. Rev. Lett. **21** (1968) 244.

[29] P. d'Argent *et al.*, *Amplitude Analyses of $D^0 \to \pi^+\pi^-\pi^+\pi^-$ and $D^0 \to K^+K^-\pi^+\pi^-$ Decays*, JHEP **05** (2017) 143, arXiv:1703.08505.

[30] CMD-2 collaboration, R. R. Akhmetshin *et al.*, *Measurement of $e^+e^- \to \pi^+\pi^-$ cross-section with CMD-2 around rho meson*, Phys. Lett. **B527** (2002) 161, arXiv:hep-ex/0112031.

[31] LHCb collaboration, R. Aaij *et al.*, *Search for CP violation through an amplitude analysis of $D^0 \to K^+K^-\pi^+\pi^-$ decays* , JHEP **02** (2019) 126, arXiv:1811.08304.

[32] C. Zemach, *Use of angular momentum tensors*, Phys. Rev. **140** (1965) B97.

[33] W. Rarita and J. Schwinger, *On a theory of particles with half integral spin*, Phys. Rev. **60** (1941) 61.

[34] S. U. Chung, *General formulation of covariant helicity-coupling amplitudes*, Phys. Rev. D **57** (1998) 431.

[35] B. S. Zou and D. V. Bugg, *Covariant tensor formalism for partial wave analyses of ψ decay to mesons*, Eur. Phys. J. **A16** (2003) 537, arXiv:hep-ph/0211457.

[36] V. Filippini, A. Fontana, and A. Rotondi, *Covariant spin tensors in meson spectroscopy*, Phys. Rev. **D51** (1995) 2247.

[37] J. Rademacker, P. d'Argent, and J. Dalseno, *Mint2*, doi: 10.5281/zenodo.2585535.

[38] T. D. Lee, R. Oehme, and C. N. Yang, *Remarks on possible noninvariance under time reversal and charge conjugation*, Phys. Rev. **106** (1957) 340.

[39] I. Dunietz, R. Fleischer, and U. Nierste, *In pursuit of new physics with B_s decays*, Phys. Rev. **D63** (2001) 114015, arXiv:hep-ph/0012219.

[40] M. Artuso, G. Borissov, and A. Lenz, *CP violation in the B_s^0 system*, Rev. Mod. Phys. **88** (2016) 045002, arXiv:1511.09466.

[41] I. Dunietz and R. G. Sachs, *Asymmetry between inclusive charmed and anticharmed modes in B^0, $\overline{B}^0$ decay as a measure of CP violation*, Phys. Rev. D **37** (1988) 3186.

[42] LHCb collaboration, R. Aaij *et al.*, *Measurement of the flavour-specific CP-violating asymmetry $a^s_{\rm sl}$ in B^0_s decays*, Phys. Lett. **B728** (2014) 607, arXiv:1308.1048.

[43] LHCb collaboration, A. A. Alves Jr. *et al.*, *The LHCb detector at the LHC*, JINST **3** (2008) S08005.

[44] LHCb collaboration, R. Aaij *et al.*, *LHCb detector performance*, Int. J. Mod. Phys. **A30** (2015) 1530022, arXiv:1412.6352.

[45] R. Aaij *et al.*, *Performance of the LHCb Vertex Locator*, JINST **9** (2014) P09007, arXiv:1405.7808.

[46] R. Arink *et al.*, *Performance of the LHCb Outer Tracker*, JINST **9** (2014) P01002, arXiv:1311.3893.

[47] P. d'Argent *et al.*, *Improved performance of the LHCb Outer Tracker in LHC Run 2*, JINST **12** (2017) P11016, arXiv:1708.00819.

[48] M. Adinolfi *et al.*, *Performance of the LHCb RICH detector at the LHC*, Eur. Phys. J. **C73** (2013) 2431, arXiv:1211.6759.

[49] R. Aaij *et al.*, *The LHCb trigger and its performance in 2011*, JINST **8** (2013) P04022, arXiv:1211.3055.

[50] V. V. Gligorov and M. Williams, *Efficient, reliable and fast high-level triggering using a bonsai boosted decision tree*, JINST **8** (2013) P02013, arXiv:1210.6861.

[51] T. Sjöstrand, S. Mrenna, and P. Skands, *PYTHIA 6.4 physics and manual*, JHEP **05** (2006) 026, arXiv:hep-ph/0603175; T. Sjöstrand, S. Mrenna, and P. Skands, *A brief introduction to PYTHIA 8.1*, Comput. Phys. Commun. **178** (2008) 852, arXiv:0710.3820.

[52] I. Belyaev *et al.*, *Handling of the generation of primary events in Gauss, the LHCb simulation framework*, J. Phys. Conf. Ser. **331** (2011) 032047.

[53] D. J. Lange, *The EvtGen particle decay simulation package*, Nucl. Instrum. Meth. **A462** (2001) 152.

[54] P. Golonka and Z. Was, *PHOTOS Monte Carlo: A precision tool for QED corrections in Z and W decays*, Eur. Phys. J. **C45** (2006) 97, arXiv:hep-ph/0506026.

[55] Geant4 collaboration, J. Allison *et al.*, *Geant4 developments and applications*, IEEE Trans. Nucl. Sci. **53** (2006) 270; Geant4 collaboration, S. Agostinelli *et al.*, *Geant4: A simulation toolkit*, Nucl. Instrum. Meth. **A506** (2003) 250.

[56] M. Clemencic *et al.*, *The LHCb simulation application, Gauss: Design, evolution and experience*, J. Phys. Conf. Ser. **331** (2011) 032023.

[57] W. D. Hulsbergen, *Decay chain fitting with a Kalman filter*, Nucl. Instrum. Meth. **A552** (2005) 566, arXiv:physics/0503191.

[58] LHCb collaboration, R. Aaij *et al.*, *Measurement of the CP asymmetry in B_s^0–$\overline{B}_s^0$ mixing*, Phys. Rev. Lett. **117** (2016) 061803, arXiv:1605.09768.

[59] L. Breiman, J. H. Friedman, R. A. Olshen, and C. J. Stone, *Classification and regression trees*, Wadsworth international group, Belmont, California, USA, 1984.

[60] Y. Freund and R. E. Schapire, *A decision-theoretic generalization of on-line learning and an application to boosting*, J. Comput. Syst. Sci. **55** (1997) 119.

[61] N. L. Johnson, *Systems of frequency curves generated by methods of translation*, Biometrika **36** (1949) 149.

[62] L. Anderlini *et al.*, *The PIDCalib package*, LHCb-PUB-2016-021, 2016.

[63] M. Pivk and F. R. Le Diberder, *sPlot: A statistical tool to unfold data distributions*, Nucl. Instrum. Meth. **A555** (2005) 356, arXiv:physics/0402083.

[64] Y. Xie, *sFit: a method for background subtraction in maximum likelihood fit*, arXiv:0905.0724.

[65] LHCb collaboration, R. Aaij *et al.*, *Opposite-side flavour tagging of B mesons at the LHCb experiment*, Eur. Phys. J. **C72** (2012) 2022, arXiv:1202.4979.

[66] LHCb collaboration, R. Aaij *et al.*, *B flavour tagging using charm decays at the LHCb experiment*, JINST **10** (2015) P10005, arXiv:1507.07892.

[67] LHCb collaboration, R. Aaij *et al.*, *A new algorithm for identifying the flavour of B_s^0 mesons at LHCb*, JINST **11** (2016) P05010, arXiv:1602.07252.

[68] LHCb collaboration, R. Aaij *et al.*, *Precision measurement of the B_s^0–$\overline{B}_s^0$ oscillation frequency in the decay $B_s^0 \to D_s^- \pi^+$*, New J. Phys. **15** (2013) 053021, arXiv:1304.4741.

[69] LHCb collaboration, R. Aaij *et al.*, *Measurement of CP violation in $B^0 \to D^\pm \pi^\mp$ decays*, JHEP **06** (2018) 084, arXiv:1805.03448.

[70] G. Punzi, *Comments on likelihood fits with variable resolution*, eConf **C030908** (2003) WELT002, arXiv:physics/0401045.

[71] *Geometric Modeling with Splines: An Introduction*, A. K. Peters, Ltd., Natick, MA, USA, 2001.

[72] P. L. Butzer, M. Schmidt, and E. L. Stark, *Observations on the history of central b-splines*, Archive for History of Exact Sciences **39** (1988) 137.

[73] T. M. Karbach, G. Raven, and M. Schiller, *Decay time integrals in neutral meson mixing and their efficient evaluation*, arXiv:1407.0748.

[74] D. Fazzini, *Flavour Tagging in the LHCb experiment*, in *Proceedings, 6th Large Hadron Collider Physics Conference (LHCP 2018): Bologna, Italy, June 4-9, 2018*, **LHCP2018** 230, 2018.

[75] LHCb collaboration, R. Aaij *et al.*, *Measurement of B^0, B_s^0, B^+ and Λ_b^0 production asymmetries in 7 and 8 TeV proton-proton collisions*, Phys. Lett. **B774** (2017) 139, arXiv:1703.08464.

[76] A. Davis *et al.*, *Measurement of the instrumental asymmetry for $K^-\pi^+$-pairs at LHCb in Run 2*, LHCb-PUB-2018-004, 2018.

[77] MARK-III collaboration, D. Coffman *et al.*, *Resonant substructure in $\overline{K}\pi\pi\pi$ decays of D mesons*, Phys. Rev. **D45** (1992) 2196.

[78] FOCUS collaboration, J. M. Link *et al.*, *Study of the $D^0 \to \pi^-\pi^+\pi^-\pi^+$ decay*, Phys. Rev. **D75** (2007) 052003, arXiv:hep-ex/0701001.

[79] CLEO collaboration, M. Artuso *et al.*, *Amplitude analysis of $D^0 \to K^+K^-\pi^+\pi^-$*, Phys. Rev. **D85** (2012) 122002, arXiv:1201.5716.

[80] R. Tibshirani, *Regression shrinkage and selection via the Lasso*, Journal of the Royal Statistical Society, Series B **58** (1994) 267.

[81] B. Guegan, J. Hardin, J. Stevens, and M. Williams, *Model selection for amplitude analysis*, JINST **10** (2015) P09002, arXiv:1505.05133.

[82] G. Schwarz, *Estimating the dimension of a model*, Ann. Statist. **6** (1978) 461.

[83] M. Kenzie *et al.*, *GammaCombo: A statistical analysis framework for combining measurements, fitting datasets and producing confidence intervals*, doi: 10.5281/zenodo.3371421; LHCb collaboration, R. Aaij *et al.*, *Measurement of the CKM angle γ from a combination of LHCb results*, JHEP **12** (2016) 087, arXiv:1611.03076.

[84] D. King, A. Lenz, and T. Rauh, *B_s mixing observables and $|V_{td}/V_{ts}|$ from sum rules*, JHEP **05** (2019) 034, arXiv:1904.00940.

[85] LHCb collaboration, R. Aaij *et al.*, *Studies of the resonance structure in $D^0 \to K^{\mp}\pi^{\pm}\pi^+\pi^-$ decays*, Eur. Phys. J. **C78** (2018) 443, arXiv:1712.08609.

LHCb collaboration

R. Aaij[31], C. Abellán Beteta[49], T. Ackernley[59], B. Adeva[45], M. Adinolfi[53], H. Afsharnia[9], C.A. Aidala[84], S. Aiola[25], Z. Ajaltouni[9], S. Akar[64], J. Albrecht[14], F. Alessio[47], M. Alexander[58], A. Alfonso Albero[44], Z. Aliouche[61], G. Alkhazov[37], P. Alvarez Cartelle[47], S. Amato[2], Y. Amhis[11], L. An[21], L. Anderlini[21], A. Andreianov[37], M. Andreotti[20], F. Archilli[16], A. Artamonov[43], M. Artuso[67], K. Arzymatov[41], E. Aslanides[10], M. Atzeni[49], B. Audurier[11], S. Bachmann[16], M. Bachmayer[48], J.J. Back[55], S. Baker[60], P. Baladron Rodriguez[45], V. Balagura[11], W. Baldini[20], J. Baptista Leite[1], R.J. Barlow[61], S. Barsuk[11], W. Barter[60], M. Bartolini[23,i], F. Baryshnikov[80], J.M. Basels[13], G. Bassi[28], B. Batsukh[67], A. Battig[14], A. Bay[48], M. Becker[14], F. Bedeschi[28], I. Bediaga[1], A. Beiter[67], V. Belavin[41], S. Belin[26], V. Bellee[48], K. Belous[43], I. Belov[39], I. Belyaev[38], G. Bencivenni[22], E. Ben-Haim[12], A. Berezhnoy[39], R. Bernet[49], D. Berninghoff[16], H.C. Bernstein[67], C. Bertella[47], E. Bertholet[12], A. Bertolin[27], C. Betancourt[49], F. Betti[19,e], M.O. Bettler[54], Ia. Bezshyiko[49], S. Bhasin[53], J. Bhom[33], L. Bian[72], M.S. Bieker[14], S. Bifani[52], P. Billoir[12], M. Birch[60], F.C.R. Bishop[54], A. Bizzeti[21,s], M. Bjørn[62], M.P. Blago[47], T. Blake[55], F. Blanc[48], S. Blusk[67], D. Bobulska[58], J.A. Boelhauve[14], O. Boente Garcia[45], T. Boettcher[63], A. Boldyrev[81], A. Bondar[42], N. Bondar[37], S. Borghi[61], M. Borisyak[41], M. Borsato[16], J.T. Borsuk[33], S.A. Bouchiba[48], T.J.V. Bowcock[59], A. Boyer[47], C. Bozzi[20], M.J. Bradley[60], S. Braun[65], A. Brea Rodriguez[45], M. Brodski[47], J. Brodzicka[33], A. Brossa Gonzalo[55], D. Brundu[26], A. Buonaura[49], C. Burr[47], A. Bursche[26], A. Butkevich[40], J.S. Butter[31], J. Buytaert[47], W. Byczynski[47], S. Cadeddu[26], H. Cai[72], R. Calabrese[20,g], L. Calefice[14,12], L. Calero Diaz[22], S. Cali[22], R. Calladine[52], M. Calvi[24,j], M. Calvo Gomez[83], P. Camargo Magalhaes[53], A. Camboni[44], P. Campana[22], D.H. Campora Perez[47], A.F. Campoverde Quezada[5], S. Capelli[24,j], L. Capriotti[19,e], A. Carbone[19,e], G. Carboni[29], R. Cardinale[23,i], A. Cardini[26], I. Carli[6], P. Carniti[24,j], L. Carus[13], K. Carvalho Akiba[31], A. Casais Vidal[45], G. Casse[59], M. Cattaneo[47], G. Cavallero[47], S. Celani[48], J. Cerasoli[10], A.J. Chadwick[59], M.G. Chapman[53], M. Charles[12], Ph. Charpentier[47], G. Chatzikonstantinidis[52], C.A. Chavez Barajas[59], M. Chefdeville[8], C. Chen[3], S. Chen[26], A. Chernov[33], S.-G. Chitic[47], V. Chobanova[45], S. Cholak[48], M. Chrzaszcz[33], A. Chubykin[37], V. Chulikov[37], P. Ciambrone[22], M.F. Cicala[55], X. Cid Vidal[45], G. Ciezarek[47], P.E.L. Clarke[57], M. Clemencic[47], H.V. Cliff[54], J. Closier[47], J.L. Cobbledick[61], V. Coco[47], J.A.B. Coelho[11], J. Cogan[10], E. Cogneras[9], L. Cojocariu[36], P. Collins[47], T. Colombo[47], L. Congedo[18,d], A. Contu[26], N. Cooke[52], G. Coombs[58], G. Corti[47], C.M. Costa Sobral[55], B. Couturier[47], D.C. Craik[63], J. Crkovská[66], M. Cruz Torres[1], R. Currie[57], C.L. Da Silva[66], E. Dall'Occo[14], J. Dalseno[45], C. D'Ambrosio[47], A. Danilina[38], P. d'Argent[47], A. Davis[61], O. De Aguiar Francisco[61], K. De Bruyn[77], S. De Capua[61], M. De Cian[48], J.M. De Miranda[1], L. De Paula[2], M. De Serio[18,d], D. De Simone[49], P. De Simone[22], J.A. de Vries[78], C.T. Dean[66], W. Dean[84], D. Decamp[8], L. Del Buono[12], B. Delaney[54], H.-P. Dembinski[14], A. Dendek[34], V. Denysenko[49], D. Derkach[81], O. Deschamps[9], F. Desse[11], F. Dettori[26,f], B. Dey[72], P. Di Nezza[22], S. Didenko[80], L. Dieste Maronas[45], H. Dijkstra[47], V. Dobishuk[51], A.M. Donohoe[17], F. Dordei[26], A.C. dos Reis[1], L. Douglas[58], A. Dovbnya[50], A.G. Downes[8], K. Dreimanis[59], M.W. Dudek[33], L. Dufour[47], V. Duk[76], P. Durante[47], J.M. Durham[66], D. Dutta[61], M. Dziewiecki[16], A. Dziurda[33], A. Dzyuba[37], S. Easo[56], U. Egede[68], V. Egorychev[38], S. Eidelman[42,v], S. Eisenhardt[57], S. Ek-In[48], L. Eklund[58], S. Ely[67], A. Ene[36], E. Epple[66], S. Escher[13], J. Eschle[49], S. Esen[31], T. Evans[47], A. Falabella[19], J. Fan[3], Y. Fan[5], B. Fang[72], N. Farley[52], S. Farry[59], D. Fazzini[24,j], P. Fedin[38], M. Féo[47], P. Fernandez Declara[47], A. Fernandez Prieto[45], J.M. Fernandez-tenllado Arribas[44], F. Ferrari[19,e], L. Ferreira Lopes[48], F. Ferreira Rodrigues[2], S. Ferreres Sole[31], M. Ferrillo[49], M. Ferro-Luzzi[47], S. Filippov[40], R.A. Fini[18], M. Fiorini[20,g], M. Firlej[34], K.M. Fischer[62], C. Fitzpatrick[61], T. Fiutowski[34], F. Fleuret[11,b], M. Fontana[12], F. Fontanelli[23,i], R. Forty[47], V. Franco Lima[59],

M. Franco Sevilla[65], M. Frank[47], E. Franzoso[20], G. Frau[16], C. Frei[47], D.A. Friday[58], J. Fu[25], Q. Fuehring[14], W. Funk[47], E. Gabriel[31], T. Gaintseva[41], A. Gallas Torreira[45], D. Galli[19,e], S. Gambetta[57,47], Y. Gan[3], M. Gandelman[2], P. Gandini[25], Y. Gao[4], M. Garau[26], L.M. Garcia Martin[55], P. Garcia Moreno[44], J. García Pardiñas[49], B. Garcia Plana[45], F.A. Garcia Rosales[11], L. Garrido[44], C. Gaspar[47], R.E. Geertsema[31], D. Gerick[16], L.L. Gerken[14], E. Gersabeck[61], M. Gersabeck[61], T. Gershon[55], D. Gerstel[10], Ph. Ghez[8], V. Gibson[54], M. Giovannetti[22,k], A. Gioventù[45], P. Gironella Gironell[44], L. Giubega[36], C. Giugliano[20,47,g], K. Gizdov[57], E.L. Gkougkousis[47], V.V. Gligorov[12], C. Göbel[69], E. Golobardes[83], D. Golubkov[38], A. Golutvin[60,80], A. Gomes[1,a], S. Gomez Fernandez[44], F. Goncalves Abrantes[69], M. Goncerz[33], G. Gong[3], P. Gorbounov[38], I.V. Gorelov[39], C. Gotti[24,j], E. Govorkova[47], J.P. Grabowski[16], R. Graciani Diaz[44], T. Grammatico[12], L.A. Granado Cardoso[47], E. Graugés[44], E. Graverini[48], G. Graziani[21], A. Grecu[36], L.M. Greeven[31], P. Griffith[20], L. Grillo[61], S. Gromov[80], B.R. Gruberg Cazon[62], C. Gu[3], M. Guarise[20], P. A. Günther[16], E. Gushchin[40], A. Guth[13], Y. Guz[43,47], T. Gys[47], T. Hadavizadeh[68], G. Haefeli[48], C. Haen[47], J. Haimberger[47], S.C. Haines[54], T. Halewood-leagas[59], P.M. Hamilton[65], Q. Han[7], X. Han[16], T.H. Hancock[62], S. Hansmann-Menzemer[16], N. Harnew[62], T. Harrison[59], C. Hasse[47], M. Hatch[47], J. He[5], M. Hecker[60], K. Heijhoff[31], K. Heinicke[14], A.M. Hennequin[47], K. Hennessy[59], L. Henry[25,46], J. Heuel[13], A. Hicheur[2], D. Hill[62], M. Hilton[61], S.E. Hollitt[14], J. Hu[16], J. Hu[71], W. Hu[7], W. Huang[5], X. Huang[72], W. Hulsbergen[31], R.J. Hunter[55], M. Hushchyn[81], D. Hutchcroft[59], D. Hynds[31], P. Ibis[14], M. Idzik[34], D. Ilin[37], P. Ilten[64], A. Inglessi[37], A. Ishteev[80], K. Ivshin[37], R. Jacobsson[47], S. Jakobsen[47], E. Jans[31], B.K. Jashal[46], A. Jawahery[65], V. Jevtic[14], M. Jezabek[33], F. Jiang[3], M. John[62], D. Johnson[47], C.R. Jones[54], T.P. Jones[55], B. Jost[47], N. Jurik[47], S. Kandybei[50], Y. Kang[3], M. Karacson[47], M. Karpov[81], N. Kazeev[81], M. Kecke[16], F. Keizer[54,47], M. Kenzie[55], T. Ketel[32], B. Khanji[14], A. Kharisova[82], S. Kholodenko[43], K.E. Kim[67], T. Kirn[13], V.S. Kirsebom[48], O. Kitouni[63], S. Klaver[31], K. Klimaszewski[35], S. Koliiev[51], A. Kondybayeva[80], A. Konoplyannikov[38], P. Kopciewicz[34], R. Kopecna[16], P. Koppenburg[31], M. Korolev[39], I. Kostiuk[31,51], O. Kot[51], S. Kotriakhova[37,30], P. Kravchenko[37], L. Kravchuk[40], R.D. Krawczyk[47], M. Kreps[55], F. Kress[60], S. Kretzschmar[13], P. Krokovny[42,v], W. Krupa[34], W. Krzemien[35], W. Kucewicz[33,l], M. Kucharczyk[33], V. Kudryavtsev[42,v], H.S. Kuindersma[31], G.J. Kunde[66], T. Kvaratskheliya[38], D. Lacarrere[47], G. Lafferty[61], A. Lai[26], A. Lampis[26], D. Lancierini[49], J.J. Lane[61], R. Lane[53], G. Lanfranchi[22], C. Langenbruch[13], J. Langer[14], O. Lantwin[49,80], T. Latham[55], F. Lazzari[28,t], R. Le Gac[10], S.H. Lee[84], R. Lefèvre[9], A. Leflat[39], S. Legotin[80], O. Leroy[10], T. Lesiak[33], B. Leverington[16], H. Li[71], L. Li[62], P. Li[16], X. Li[66], Y. Li[6], Y. Li[6], Z. Li[67], X. Liang[67], T. Lin[60], R. Lindner[47], V. Lisovskyi[14], R. Litvinov[26], G. Liu[71], H. Liu[5], S. Liu[6], X. Liu[3], A. Loi[26], J. Lomba Castro[45], I. Longstaff[58], J.H. Lopes[2], G. Loustau[49], G.H. Lovell[54], Y. Lu[6], D. Lucchesi[27,m], S. Luchuk[40], M. Lucio Martinez[31], V. Lukashenko[31], Y. Luo[3], A. Lupato[61], E. Luppi[20,g], O. Lupton[55], A. Lusiani[28,r], X. Lyu[5], L. Ma[6], S. Maccolini[19,e], F. Machefert[11], F. Maciuc[36], V. Macko[48], P. Mackowiak[14], S. Maddrell-Mander[53], O. Madejczyk[34], L.R. Madhan Mohan[53], O. Maev[37], A. Maevskiy[81], D. Maisuzenko[37], M.W. Majewski[34], J.J. Malczewski[33], S. Malde[62], B. Malecki[47], A. Malinin[79], T. Maltsev[42,v], H. Malygina[16], G. Manca[26,f], G. Mancinelli[10], R. Manera Escalero[44], D. Manuzzi[19,e], D. Marangotto[25,o], J. Maratas[9,u], J.F. Marchand[8], U. Marconi[19], S. Mariani[21,47,h], C. Marin Benito[11], M. Marinangeli[48], P. Marino[48], J. Marks[16], P.J. Marshall[59], G. Martellotti[30], L. Martinazzoli[47,j], M. Martinelli[24,j], D. Martinez Santos[45], F. Martinez Vidal[46], A. Massafferri[1], M. Materok[13], R. Matev[47], A. Mathad[49], Z. Mathe[47], V. Matiunin[38], C. Matteuzzi[24], K.R. Mattioli[84], A. Mauri[31], E. Maurice[11,b], J. Mauricio[44], M. Mazurek[35], M. McCann[60], L. Mcconnell[17], T.H. Mcgrath[61], A. McNab[61], R. McNulty[17], J.V. Mead[59], B. Meadows[64], C. Meaux[10], G. Meier[14], N. Meinert[75], D. Melnychuk[35], S. Meloni[24,j], M. Merk[31,78], A. Merli[25], L. Meyer Garcia[2], M. Mikhasenko[47], D.A. Milanes[73], E. Millard[55], M. Milovanovic[47], M.-N. Minard[8], L. Minzoni[20,g], S.E. Mitchell[57], B. Mitreska[61],

D.S. Mitzel[47], A. Mödden[14], R.A. Mohammed[62], R.D. Moise[60], T. Mombächer[14], I.A. Monroy[73], S. Monteil[9], M. Morandin[27], G. Morello[22], M.J. Morello[28,r], J. Moron[34], A.B. Morris[74], A.G. Morris[55], R. Mountain[67], H. Mu[3], F. Muheim[57], M. Mukherjee[7], M. Mulder[47], D. Müller[47], K. Müller[49], C.H. Murphy[62], D. Murray[61], P. Muzzetto[26,47], P. Naik[53], T. Nakada[48], R. Nandakumar[56], T. Nanut[48], I. Nasteva[2], M. Needham[57], I. Neri[20,g], N. Neri[25,o], S. Neubert[74], N. Neufeld[47], R. Newcombe[60], T.D. Nguyen[48], C. Nguyen-Mau[48], E.M. Niel[11], S. Nieswand[13], N. Nikitin[39], N.S. Nolte[47], C. Nunez[84], A. Oblakowska-Mucha[34], V. Obraztsov[43], D.P. O'Hanlon[53], R. Oldeman[26,f], M.E. Olivares[67], C.J.G. Onderwater[77], A. Ossowska[33], J.M. Otalora Goicochea[2], T. Ovsiannikova[38], P. Owen[49], A. Oyanguren[46,47], B. Pagare[55], P.R. Pais[47], T. Pajero[28,47,r], A. Palano[18], M. Palutan[22], Y. Pan[61], G. Panshin[82], A. Papanestis[56], M. Pappagallo[18,d], L.L. Pappalardo[20,g], C. Pappenheimer[64], W. Parker[65], C. Parkes[61], C.J. Parkinson[45], B. Passalacqua[20], G. Passaleva[21], A. Pastore[18], M. Patel[60], C. Patrignani[19,e], C.J. Pawley[78], A. Pearce[47], A. Pellegrino[31], M. Pepe Altarelli[47], S. Perazzini[19], D. Pereima[38], P. Perret[9], K. Petridis[53], A. Petrolini[23,i], A. Petrov[79], S. Petrucci[57], M. Petruzzo[25], T.T.H. Pham[67], A. Philippov[41], L. Pica[28], M. Piccini[76], B. Pietrzyk[8], G. Pietrzyk[48], M. Pili[62], D. Pinci[30], F. Pisani[47], A. Piucci[16], Resmi P.K[10], V. Placinta[36], J. Plews[52], M. Plo Casasus[45], F. Polci[12], M. Poli Lener[22], M. Poliakova[67], A. Poluektov[10], N. Polukhina[80,c], I. Polyakov[67], E. Polycarpo[2], G.J. Pomery[53], S. Ponce[47], D. Popov[5,47], S. Popov[41], S. Poslavskii[43], K. Prasanth[33], L. Promberger[47], C. Prouve[45], V. Pugatch[51], H. Pullen[62], G. Punzi[28,n], W. Qian[5], J. Qin[5], R. Quagliani[12], B. Quintana[8], N.V. Raab[17], R.I. Rabadan Trejo[10], B. Rachwal[34], J.H. Rademacker[53], M. Rama[28], M. Ramos Pernas[55], M.S. Rangel[2], F. Ratnikov[41,81], G. Raven[32], M. Reboud[8], F. Redi[48], F. Reiss[12], C. Remon Alepuz[46], Z. Ren[3], V. Renaudin[62], R. Ribatti[28], S. Ricciardi[56], K. Rinnert[59], P. Robbe[11], A. Robert[12], G. Robertson[57], A.B. Rodrigues[48], E. Rodrigues[59], J.A. Rodriguez Lopez[73], A. Rollings[62], P. Roloff[47], V. Romanovskiy[43], M. Romero Lamas[45], A. Romero Vidal[45], J.D. Roth[84], M. Rotondo[22], M.S. Rudolph[67], T. Ruf[47], J. Ruiz Vidal[46], A. Ryzhikov[81], J. Ryzka[34], J.J. Saborido Silva[45], N. Sagidova[37], N. Sahoo[55], B. Saitta[26,f], D. Sanchez Gonzalo[44], C. Sanchez Gras[31], R. Santacesaria[30], C. Santamarina Rios[45], M. Santimaria[22], E. Santovetti[29,k], D. Saranin[80], G. Sarpis[58], M. Sarpis[74], A. Sarti[30], C. Satriano[30,q], A. Satta[29], M. Saur[5], D. Savrina[38,39], H. Sazak[9], L.G. Scantlebury Smead[62], S. Schael[13], M. Schellenberg[14], M. Schiller[58], H. Schindler[47], M. Schmelling[15], T. Schmelzer[14], B. Schmidt[47], O. Schneider[48], A. Schopper[47], M. Schubiger[31], S. Schulte[48], M.H. Schune[11], R. Schwemmer[47], B. Sciascia[22], A. Sciubba[30], S. Sellam[45], A. Semennikov[38], M. Senghi Soares[32], A. Sergi[52,47], N. Serra[49], L. Sestini[27], A. Seuthe[14], P. Seyfert[47], D.M. Shangase[84], M. Shapkin[43], I. Shchemerov[80], L. Shchutska[48], T. Shears[59], L. Shekhtman[42,v], Z. Shen[4], V. Shevchenko[79], E.B. Shields[24,j], E. Shmanin[80], J.D. Shupperd[67], B.G. Siddi[20], R. Silva Coutinho[49], G. Simi[27], S. Simone[18,d], I. Skiba[20,g], N. Skidmore[74], T. Skwarnicki[67], M.W. Slater[52], J.C. Smallwood[62], J.G. Smeaton[54], A. Smetkina[38], E. Smith[13], M. Smith[60], A. Snoch[31], M. Soares[19], L. Soares Lavra[9], M.D. Sokoloff[64], F.J.P. Soler[58], A. Solovev[37], I. Solovyev[37], F.L. Souza De Almeida[2], B. Souza De Paula[2], B. Spaan[14], E. Spadaro Norella[25,o], P. Spradlin[58], F. Stagni[47], M. Stahl[64], S. Stahl[47], P. Stefko[48], O. Steinkamp[49,80], S. Stemmle[16], O. Stenyakin[43], H. Stevens[14], S. Stone[67], M.E. Stramaglia[48], M. Straticiuc[36], D. Strekalina[80], S. Strokov[82], F. Suljik[62], J. Sun[26], L. Sun[72], Y. Sun[65], P. Svihra[61], P.N. Swallow[52], K. Swientek[34], A. Szabelski[35], T. Szumlak[34], M. Szymanski[47], S. Taneja[61], F. Teubert[47], E. Thomas[47], K.A. Thomson[59], M.J. Tilley[60], V. Tisserand[9], S. T'Jampens[8], M. Tobin[6], S. Tolk[47], L. Tomassetti[20,g], D. Torres Machado[1], D.Y. Tou[12], M. Traill[58], M.T. Tran[48], E. Trifonova[80], C. Trippl[48], G. Tuci[28,n], A. Tully[48], N. Tuning[31], A. Ukleja[35], D.J. Unverzagt[16], A. Usachov[31], A. Ustyuzhanin[41,81], U. Uwer[16], A. Vagner[82], V. Vagnoni[19], A. Valassi[47], G. Valenti[19], N. Valls Canudas[44], M. van Beuzekom[31], M. Van Dijk[48], H. Van Hecke[66], E. van Herwijnen[80], C.B. Van Hulse[17], M. van Veghel[77],

R. Vazquez Gomez[45], P. Vazquez Regueiro[45], C. Vázquez Sierra[31], S. Vecchi[20], J.J. Velthuis[53], M. Veltri[21,p], A. Venkateswaran[67], M. Veronesi[31], M. Vesterinen[55], D. Vieira[64], M. Vieites Diaz[48], H. Viemann[75], X. Vilasis-Cardona[83], E. Vilella Figueras[59], P. Vincent[12], G. Vitali[28], A. Vollhardt[49], D. Vom Bruch[12], A. Vorobyev[37], V. Vorobyev[42,v], N. Voropaev[37], R. Waldi[75], J. Walsh[28], C. Wang[16], J. Wang[3], J. Wang[72], J. Wang[4], J. Wang[6], M. Wang[3], R. Wang[53], Y. Wang[7], Z. Wang[49], H.M. Wark[59], N.K. Watson[52], S.G. Weber[12], D. Websdale[60], C. Weisser[63], B.D.C. Westhenry[53], D.J. White[61], M. Whitehead[53], D. Wiedner[14], G. Wilkinson[62], M. Wilkinson[67], I. Williams[54], M. Williams[63,68], M.R.J. Williams[57], F.F. Wilson[56], W. Wislicki[35], M. Witek[33], L. Witola[16], G. Wormser[11], S.A. Wotton[54], H. Wu[67], K. Wyllie[47], Z. Xiang[5], D. Xiao[7], Y. Xie[7], A. Xu[4], J. Xu[5], L. Xu[3], M. Xu[7], Q. Xu[5], Z. Xu[5], Z. Xu[4], D. Yang[3], Y. Yang[5], Z. Yang[3], Z. Yang[65], Y. Yao[67], L.E. Yeomans[59], H. Yin[7], J. Yu[70], X. Yuan[67], O. Yushchenko[43], E. Zaffaroni[48], K.A. Zarebski[52], M. Zavertyaev[15,c], M. Zdybal[33], O. Zenaiev[47], M. Zeng[3], D. Zhang[7], L. Zhang[3], S. Zhang[4], Y. Zhang[4], Y. Zhang[62], A. Zhelezov[16], Y. Zheng[5], X. Zhou[5], Y. Zhou[5], X. Zhu[3], V. Zhukov[13,39], J.B. Zonneveld[57], S. Zucchelli[19,e], D. Zuliani[27], G. Zunica[61].

[1] *Centro Brasileiro de Pesquisas Físicas (CBPF), Rio de Janeiro, Brazil*
[2] *Universidade Federal do Rio de Janeiro (UFRJ), Rio de Janeiro, Brazil*
[3] *Center for High Energy Physics, Tsinghua University, Beijing, China*
[4] *School of Physics State Key Laboratory of Nuclear Physics and Technology, Peking University, Beijing, China*
[5] *University of Chinese Academy of Sciences, Beijing, China*
[6] *Institute Of High Energy Physics (IHEP), Beijing, China*
[7] *Institute of Particle Physics, Central China Normal University, Wuhan, Hubei, China*
[8] *Univ. Grenoble Alpes, Univ. Savoie Mont Blanc, CNRS, IN2P3-LAPP, Annecy, France*
[9] *Université Clermont Auvergne, CNRS/IN2P3, LPC, Clermont-Ferrand, France*
[10] *Aix Marseille Univ, CNRS/IN2P3, CPPM, Marseille, France*
[11] *Université Paris-Saclay, CNRS/IN2P3, IJCLab, Orsay, France*
[12] *LPNHE, Sorbonne Université, Paris Diderot Sorbonne Paris Cité, CNRS/IN2P3, Paris, France*
[13] *I. Physikalisches Institut, RWTH Aachen University, Aachen, Germany*
[14] *Fakultät Physik, Technische Universität Dortmund, Dortmund, Germany*
[15] *Max-Planck-Institut für Kernphysik (MPIK), Heidelberg, Germany*
[16] *Physikalisches Institut, Ruprecht-Karls-Universität Heidelberg, Heidelberg, Germany*
[17] *School of Physics, University College Dublin, Dublin, Ireland*
[18] *INFN Sezione di Bari, Bari, Italy*
[19] *INFN Sezione di Bologna, Bologna, Italy*
[20] *INFN Sezione di Ferrara, Ferrara, Italy*
[21] *INFN Sezione di Firenze, Firenze, Italy*
[22] *INFN Laboratori Nazionali di Frascati, Frascati, Italy*
[23] *INFN Sezione di Genova, Genova, Italy*
[24] *INFN Sezione di Milano-Bicocca, Milano, Italy*
[25] *INFN Sezione di Milano, Milano, Italy*
[26] *INFN Sezione di Cagliari, Monserrato, Italy*
[27] *Universita degli Studi di Padova, Universita e INFN, Padova, Padova, Italy*
[28] *INFN Sezione di Pisa, Pisa, Italy*
[29] *INFN Sezione di Roma Tor Vergata, Roma, Italy*
[30] *INFN Sezione di Roma La Sapienza, Roma, Italy*
[31] *Nikhef National Institute for Subatomic Physics, Amsterdam, Netherlands*
[32] *Nikhef National Institute for Subatomic Physics and VU University Amsterdam, Amsterdam, Netherlands*
[33] *Henryk Niewodniczanski Institute of Nuclear Physics Polish Academy of Sciences, Kraków, Poland*
[34] *AGH - University of Science and Technology, Faculty of Physics and Applied Computer Science, Kraków, Poland*
[35] *National Center for Nuclear Research (NCBJ), Warsaw, Poland*
[36] *Horia Hulubei National Institute of Physics and Nuclear Engineering, Bucharest-Magurele, Romania*

[37] Petersburg Nuclear Physics Institute NRC Kurchatov Institute (PNPI NRC KI), Gatchina, Russia
[38] Institute of Theoretical and Experimental Physics NRC Kurchatov Institute (ITEP NRC KI), Moscow, Russia
[39] Institute of Nuclear Physics, Moscow State University (SINP MSU), Moscow, Russia
[40] Institute for Nuclear Research of the Russian Academy of Sciences (INR RAS), Moscow, Russia
[41] Yandex School of Data Analysis, Moscow, Russia
[42] Budker Institute of Nuclear Physics (SB RAS), Novosibirsk, Russia
[43] Institute for High Energy Physics NRC Kurchatov Institute (IHEP NRC KI), Protvino, Russia, Protvino, Russia
[44] ICCUB, Universitat de Barcelona, Barcelona, Spain
[45] Instituto Galego de Física de Altas Enerxías (IGFAE), Universidade de Santiago de Compostela, Santiago de Compostela, Spain
[46] Instituto de Fisica Corpuscular, Centro Mixto Universidad de Valencia - CSIC, Valencia, Spain
[47] European Organization for Nuclear Research (CERN), Geneva, Switzerland
[48] Institute of Physics, Ecole Polytechnique Fédérale de Lausanne (EPFL), Lausanne, Switzerland
[49] Physik-Institut, Universität Zürich, Zürich, Switzerland
[50] NSC Kharkiv Institute of Physics and Technology (NSC KIPT), Kharkiv, Ukraine
[51] Institute for Nuclear Research of the National Academy of Sciences (KINR), Kyiv, Ukraine
[52] University of Birmingham, Birmingham, United Kingdom
[53] H.H. Wills Physics Laboratory, University of Bristol, Bristol, United Kingdom
[54] Cavendish Laboratory, University of Cambridge, Cambridge, United Kingdom
[55] Department of Physics, University of Warwick, Coventry, United Kingdom
[56] STFC Rutherford Appleton Laboratory, Didcot, United Kingdom
[57] School of Physics and Astronomy, University of Edinburgh, Edinburgh, United Kingdom
[58] School of Physics and Astronomy, University of Glasgow, Glasgow, United Kingdom
[59] Oliver Lodge Laboratory, University of Liverpool, Liverpool, United Kingdom
[60] Imperial College London, London, United Kingdom
[61] Department of Physics and Astronomy, University of Manchester, Manchester, United Kingdom
[62] Department of Physics, University of Oxford, Oxford, United Kingdom
[63] Massachusetts Institute of Technology, Cambridge, MA, United States
[64] University of Cincinnati, Cincinnati, OH, United States
[65] University of Maryland, College Park, MD, United States
[66] Los Alamos National Laboratory (LANL), Los Alamos, United States
[67] Syracuse University, Syracuse, NY, United States
[68] School of Physics and Astronomy, Monash University, Melbourne, Australia, associated to [55]
[69] Pontifícia Universidade Católica do Rio de Janeiro (PUC-Rio), Rio de Janeiro, Brazil, associated to [2]
[70] Physics and Micro Electronic College, Hunan University, Changsha City, China, associated to [7]
[71] Guangdong Provencial Key Laboratory of Nuclear Science, Institute of Quantum Matter, South China Normal University, Guangzhou, China, associated to [3]
[72] School of Physics and Technology, Wuhan University, Wuhan, China, associated to [3]
[73] Departamento de Fisica , Universidad Nacional de Colombia, Bogota, Colombia, associated to [12]
[74] Universität Bonn - Helmholtz-Institut für Strahlen und Kernphysik, Bonn, Germany, associated to [16]
[75] Institut für Physik, Universität Rostock, Rostock, Germany, associated to [16]
[76] INFN Sezione di Perugia, Perugia, Italy, associated to [20]
[77] Van Swinderen Institute, University of Groningen, Groningen, Netherlands, associated to [31]
[78] Universiteit Maastricht, Maastricht, Netherlands, associated to [31]
[79] National Research Centre Kurchatov Institute, Moscow, Russia, associated to [38]
[80] National University of Science and Technology "MISIS", Moscow, Russia, associated to [38]
[81] National Research University Higher School of Economics, Moscow, Russia, associated to [41]
[82] National Research Tomsk Polytechnic University, Tomsk, Russia, associated to [38]
[83] DS4DS, La Salle, Universitat Ramon Llull, Barcelona, Spain, associated to [44]
[84] University of Michigan, Ann Arbor, United States, associated to [67]

[a] Universidade Federal do Triângulo Mineiro (UFTM), Uberaba-MG, Brazil
[b] Laboratoire Leprince-Ringuet, Palaiseau, France
[c] P.N. Lebedev Physical Institute, Russian Academy of Science (LPI RAS), Moscow, Russia
[d] Università di Bari, Bari, Italy

[e] *Università di Bologna, Bologna, Italy*
[f] *Università di Cagliari, Cagliari, Italy*
[g] *Università di Ferrara, Ferrara, Italy*
[h] *Università di Firenze, Firenze, Italy*
[i] *Università di Genova, Genova, Italy*
[j] *Università di Milano Bicocca, Milano, Italy*
[k] *Università di Roma Tor Vergata, Roma, Italy*
[l] *AGH - University of Science and Technology, Faculty of Computer Science, Electronics and Telecommunications, Kraków, Poland*
[m] *Università di Padova, Padova, Italy*
[n] *Università di Pisa, Pisa, Italy*
[o] *Università degli Studi di Milano, Milano, Italy*
[p] *Università di Urbino, Urbino, Italy*
[q] *Università della Basilicata, Potenza, Italy*
[r] *Scuola Normale Superiore, Pisa, Italy*
[s] *Università di Modena e Reggio Emilia, Modena, Italy*
[t] *Università di Siena, Siena, Italy*
[u] *MSU - Iligan Institute of Technology (MSU-IIT), Iligan, Philippines*
[v] *Novosibirsk State University, Novosibirsk, Russia*